Definition and Symmetry of Averaged Stress Tensor in Granular Media and its 3D DEM Inspection Under Static and Dynamic Conditions

Beichuan Yan[a,*], Richard A. Regueiro[a]

[a]*Department of Civil, Environmental, and Architectural Engineering, University of Colorado Boulder*

Abstract

The paper aims to clarify the stress tensor definition and its symmetry property that applies to granular media, and conducts 3D Discrete Element Method (DEM) inspection of the stress tensor definitions provided in the literature. Various stress tensor formulas under static and dynamic conditions are summarized, compared and numerically inspected through different types of simulation, such as gravitational deposition, isotropic/oedometer compression and high-strain-rate (HSR) oedometer impact. The stress tensor symmetry is particularly discussed from the perspective of applying classical continuum mechanics to granular media. It is proved analytically and numerically that the stress tensor should be calculated by Bagi's formula, not Weber's formula or Drescher's formula, for a particle assembly or representative volume element (RVE) in static equilibrium. We propose to modify the De Saxcé and Nicot formulas by incorporating the *boundary-radius-gap* term such that they are consistent with Bagi's formula, which is particularly well-suited for studying granular phenomena that transition between static, quasi-static and dynamic conditions.

It is shown from the perspective of stress tensor calculation that the number of particles in the RVE does not need to be large. Symmetry of averaged stress tensor can be accurately satisfied in static equilibrium of the granular DEM RVE, however it cannot in quasi-static or dynamic states due to imbalance of angular momentum of the granular DEM RVE (in comparison to the

---

*Corresponding author. Fax: +1-303-492-7317

Email addresses: `beichuan.yan@colorado.edu` (Beichuan Yan), `richard.regueiro@colorado.edu` (Richard A. Regueiro)

balance of angular momentum which is always satisfied in classical continuum mechanics). When the stress tensor definition is extended to "discontinuous" state with regard to discrete granular DEM RVEs, the calculated values need to be treated with caution.

Keywords: granular media, averaged stress tensor, symmetry and asymmetry, discrete element method, static equilibrium, dynamic conditions

1. INTRODUCTION

The microstructural definition of the averaged stress tensor over a granular particle assembly has been a controversial topic (Weber, 1966; Christoffersen et al., 1981; Rothenburg and Selvadurai, 1981; Bagi, 1996, 1999, 2003; Kuhn, 2003; Bardet and Vardoulakis, 2001; Fortin et al., 2003; De Saxcé et al., 2004; Balevičius and Markauskas, 2007; Nicot et al., 2013), and can still be regarded as an open question, especially when the dynamic effect is considered (Bagi, 1999; Fortin et al., 2003; De Saxcé et al., 2004; Nicot et al., 2013). Furthermore, when micropolar continuum theory is adopted in which a local rotation of points is incorporated as well as the translation assumed in classical continuum mechanics (CCM), the stress tensor definition becomes even more complicated and disputable (Eringen, 1968; Nowacki, 1974; Fortin et al., 2003; Nowacki and Olszak, 2014).

Weber (1966) calculated a stress tensor by averaging the contact forces in the vicinity of a spatial point, which turns out to be asymmetric. Christoffersen et al. (1981) derived the same formula for the macroscopic stress in terms of volume average of the product of contact forces and branch vectors by applying the principle of virtual work.

Drescher and De Jong (1972); Cowin (1977); Cundall and Strack (1983) presented a stress definition which considers the relation between the volume average of stress and a surface integral of traction in continuum mechanics. Such a definition is made without using the principle of virtual work.

Bagi (1996) pointed out that there are two approaches to defining the stress tensor in granular materials: (1) the continuum-mechanical approach, which treats a particle assembly as a continuous domain, accepts the concept of infinitesimally small representative volume element (RVE), and applies stress and strain as fundamental variables; and (2) microstructural approach, which finds macro-level state variables that are based on micro-variables such

2

as contact force, grain displacements and local geometrical characteristics. Approach (1) is used in conventional constitutive relationships with limited validity due to experimental condition difficulty and mathematical form complications, and approach (2) has been commonly accepted to date with the availability of high-precision 3D Discrete Element Method (DEM) and computational power. Bagi (1996) presented definitions of stress and small strain in terms of local, micro-level variables with the help of two complementary geometrical systems. Bagi (1999) presented the stress tensor definition of particle assemblies with volumetric loads in addition to boundary forces, and clearly defined branch vectors: for internal contacts, the branch vector connects the centroids of two particles; for external contact points, the branch vector points from the centroid of the boundary particle to its external contact point.

Bardet and Vardoulakis (2001) studied the stress tensor definition using virtual work in granular media. They showed that the average stress tensor is always symmetric, when it is alternately defined by using statics and no contact moment. The stress asymmetry, which results from external moments, has an amplitude that decreases with an increasing volume size. A contradictory phenomenon was found: the stress asymmetry is obtained when the stress is defined from virtual work, but is lost when the stress is defined from statics.

Bagi (2003) analyzed why Bardet and Vardoulakis (2001) found different results with the two nominally different, but theoretically equivalent, methods (static equilibrium equations versus the principle of virtual displacements), and pointed out that they replaced the discrete system with an equivalent continuum whose boundary intersects the boundary grains and goes through their centroids, when applying the principle of virtual displacements.

Bardet and Vardoulakis (2001) pointed out that symmetry of the stress tensor has significant implications in computational granular mechanics, particularly for simulations using dynamic relaxation (DR) to solve the equilibrium equations of statics: the computed asymmetry of stress tensor implies inaccurate calculation and/or lack of static equilibrium. The conclusion should also be applicable to dynamic simulations which eventually reach static equilibrium.

Fortin et al. (2003); De Saxcé et al. (2004) constructed an averaged Cauchy stress tensor for a granular medium which takes into account the contact reactions and the body forces acting at the grain level, by averaging

3

stresses from all of the individual grains to the full granular assembly. They pointed out that the constructed stress tensor is automatically symmetric and invariant by translation. In particular, "in dense granular materials, the velocity of the particles is generally small, but their acceleration and the corresponding inertia forces cannot be neglected because they balance the contact and gravity forces. Then, even for very small velocities, the contact reactions, gravity and inertia forces have the same order of magnitude and must be considered together in the calculation of the mean stress tensor." De Saxcé et al. (2004) presented a rigorous proof of the stress tensor symmetry by incorporating the equations of balance of angular momentum.

Nicot et al. (2013) studied the internal effect on stress tensor definition based on an equivalent continuum medium but using different decomposition of dynamic contributions. They concluded that the stress tensor can be expressed as a sum of two contributions: (i) the standard term by Love-Weber formula in quasi-static regime; and (ii) dynamic effects related to rotational velocities and accelerations of the particles. It is interesting to observe from their numerical simulation of silo discharge that the inertial terms of stress do not have the same order of magnitude as that of the static stress, being much lower. It should be noted that the balance of linear momentum is relied on in the derivation, whereas the balance of angular momentum is not involved.

Smith and Wensrich (2014) demonstrated that the dynamic component of stress can be further separated into two parts: a component expressed in terms of the net moment arising from contact; and a symmetric term arising from the centripetal acceleration of material within the particle.

Lin and Wu (2016) pointed out that the stress symmetry is only an assumption for macroscale problems in which the microstructure can be neglected, and "if a length scale equivalent to the particle scale is used, the stress asymmetry becomes significant comparing to other stress component. Therefore, asymmetric stress tensors should be used to obtain enhanced continuum model to describe scale dependent phenomena."

In this paper we present our work on the definition and symmetry of static and dynamic stress tensor in granular media, which serves as clarification of concepts and numerical verification of the quantities, before extending in future work the study of stress-strain relations, especially to objective rate-form stress and deformation tensors in granular media within large-scale parallel computing of 3D DEM for complex-shaped particles. Section 1 has reviewed the history of stress tensor definition for granular materials; Section 2 summarizes various formulas for the stress tensor; Section 3 compares the formulas,

4

pointing out the importance of a *boundary-radius-gap* term and uses this term to modify other formulas to achieve consistency between the formulas; Section 4 discusses the stress tensor symmetry and its premise in continuum and granular media, and proposes "in-contact" and "out-of-contact" states; Section 5 presents numerical inspection of the stress formulas and symmetry using DEM simulations that cover static, quasi-static and dynamic conditions; the last section gives conclusion and outlook.

2. ANALYTICAL STRESS TENSOR EXPRESSION

Weber (1966); Christoffersen et al. (1981); Rothenburg and Selvadurai (1981) calculated the stress tensor at a point by averaging the contact forces in the vicinity using the following formula:

$$\langle \sigma_{ij} \rangle_{Weber} = \frac{1}{V} \sum_{c \in I} f_i^c l_j^c \tag{1}$$

where V denotes volume of the RVE, c the particle contacts, and I particle contacts internal to the RVE. The force vectors f_i^c are the contact forces transmitted at the internal contacts, as illustrated in Fig.1(a), and the vectors l_j^c are the branch vectors for internal contact points which connect the centroids of two adjoining particles. Christoffersen et al. (1981) derived this formula in terms of volume average of the product of contact forces and branch vectors by applying the principle of virtual work.

Drescher and De Jong (1972); Cowin (1977); Cundall and Strack (1983) used the following stress definition which is analogous to a surface integral of traction in continuum mechanics:

$$\langle \sigma_{ij} \rangle_{Drescher} = \frac{1}{V} \sum_{e \in E} f_i^e x_j^e \tag{2}$$

where E denotes particle contacts external to or on the boundary of the RVE, f_i^e the contact force vectors on the boundary of the RVE, as shown in Fig.1(a), and x_j^e the current space coordinate vector of contact points on the boundary.

Bagi (1996, 1999, 2003) presented a stress tensor definition which includes both internal and external contact forces:

$$\langle \sigma_{ij} \rangle_{Bagi} = \frac{1}{V} \left(\sum_{c \in I} f_i^c l_j^c + \sum_{e \in E} f_i^e l_j^e \right) \tag{3}$$

5

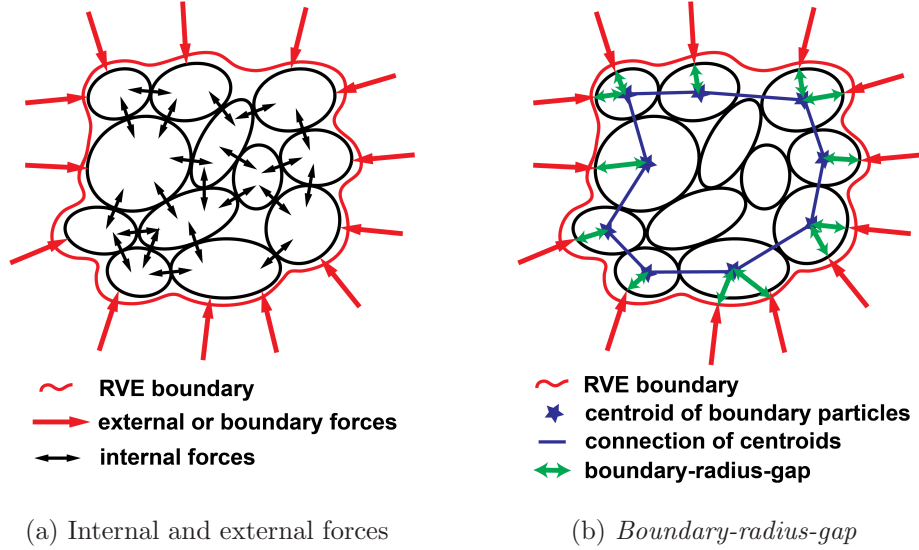(a) Internal and external forces (b) *Boundary-radius-gap*

Figure 1: Schematic of RVE.

where the forces f_i^e are the contact force vectors on the boundary of the RVE, and the vectors l_j^e are the branch vectors associated with the external contact points, also called boundary-radius gaps, which point from the centroids of the boundary particles to the external contact points, as illustrated in Fig.1(b).

Fortin et al. (2003); De Saxcé et al. (2004) constructed an averaged Cauchy stress tensor in integral form which takes into account the contact reaction forces and the body forces:

$$\langle \sigma_{ij} \rangle_{\text{De Saxcé}} = \frac{1}{V} \left(\sum_{c \in V} x_i^c f_j^c + \int_V x_i \rho \Big(g_j - a_j \Big) dV \right) \tag{4}$$

where $V = I \cup E$, f_j^c denotes internal and boundary contact force vectors, g_j the gravitational acceleration, a_j the inertial acceleration, and x_j the current spatial coordinate vector within V.

Nicot et al. (2013) derived the following stress tensor definition which takes into account inertial effect:

$$\langle \sigma_{ij} \rangle_{Nicot} = \frac{1}{V} \sum_{c \in I} f_i^c l_j^c - \frac{1}{V} \sum_{p \in V} \left(\varepsilon_{ikl} \dot{\Omega}_k^p \chi_{jl}^p + \Omega_i^p \Omega_k^p \chi_{jk}^p - (\Omega^p)^2 \chi_{ij}^p \right) \tag{5}$$

6

where $V = I \cup E$, p denotes particles within V, ε_{ikl} is the permutation symbol, Ω^p is the magnitude of angular velocity of particle 'p', and χ_{ij}^p is the inertia matrix. It should be noted that angular velocity, angular acceleration and inertia tensor are written with respect to the global coordinate system (GCS) in this equation; i.e., they must be converted into GCS if calculated in local coordinate system (LCS).

3. IMPORTANT NOTES ON THE FORMULAS

Firstly, we prove that Eq.(2) and Eq.(3) are not equivalent in static equilibrium:

$$\langle \sigma_{ij} \rangle_{Drescher} - \langle \sigma_{ij} \rangle_{Bagi} = \frac{1}{V} \sum_{p \in I, c \in I} f_i^c x_j^p \tag{6}$$

where x_j^p denotes the centroid coordinate of particle 'p', and the sets $p \in I, c \in I$ represent interior particles, which are surrounded by the outermost exterior particles. For example, there are only three of this type of particle as shown in Fig.1(b). The inequality of these two formulas is numerically verified in Section 5.3.

Secondly, Nicot et al. (2013) presented a rigorous derivation of stress tensor formula, however it is worth noting that they neglected a *boundary-radius-gap* (see Fig.1(b)) term in Eq.(5) on purpose. The term seems to be negligible with regard to other terms for specimens containing a sufficiently large number of grains. However, there are three reasons that it should not be discarded:

1. In many granular materials, the grains cover a wide range of sizes. For example, for geo-materials such as sand and gravel, the size ratio between the largest and smallest particle can be as high as 10^5. The *boundary-radius-gap* term for a large particle located on the boundary of the RVE can have significant bearing on the stress calculation, and discarding it leads to inaccurate results.

2. As shown in Section 5.2, the number of particles in a RVE does not need to be large for accurate stress tensor calculation. For example, for a $5 \times 5 \times 5$ particle cluster, the *boundary-radius-gap* can influence the stress tensor calculation appreciably.

7

3. The *boundary-radius-gap* term plays a critical role in maintaining stress symmetry, and discarding it leads to asymmetry of the stress tensor for statics. This is shown in the following sections.

We derive a modification to Eq.(5) with the *boundary-radius-gap* term incorporated. We start from Eq.(5) in Nicot et al. (2013) or Eq.(4) in De Saxcé et al. (2004). These two equations are exactly the same, and they were originally due to Chree (1892), shown by Eq.(7):

$$\langle \sigma_{ij} \rangle = \frac{1}{V} \int_{\partial V} f_i^{ext} x_j dS - \frac{1}{V} \int_V (\rho \ddot{x}_i - \gamma_i) x_j dV \tag{7}$$

where γ_i denotes the gravitational acceleration vector per unit volume, and f_i^{ext} the external traction vector.

In granular media this equation is expressed as:

$$\langle \sigma_{ij} \rangle = \frac{1}{V} \sum_{p \in \partial V} f_i^{ext,p} x_j^p - \frac{1}{V} \int_V (\rho \ddot{x}_i - \gamma_i) x_j dV \tag{8}$$

where the external force $\boldsymbol{f}^{ext,p}$ applies at $\boldsymbol{x}^p$ on boundary particle 'p'. For boundary particle 'p', $\boldsymbol{x}^p = \boldsymbol{x}^{Gp} + \boldsymbol{r}^p$, where Gp is the center of gravity of particle 'p', and $\boldsymbol{r}^p$ is the radius vector pointing from $\boldsymbol{x}^{Gp}$ to $\boldsymbol{x}^p$. Then Eq. (8) can be rewritten as:

$$\begin{aligned} \langle \sigma_{ij} \rangle =& \frac{1}{V} \sum_{p \in \partial V} f_i^{ext,p} x_j^{Gp} + \frac{1}{V} \sum_{p \in \partial V} f_i^{ext,p} r_j^p \\ &- \frac{1}{V} \int_V (\rho \ddot{x}_i - \gamma_i) x_j dV \end{aligned} \tag{9}$$

where the 2nd term on the RHS is the so called *boundary-radius-gap* term.

Following the derivation in Nicot et al. (2013) that converts the equation from boundary force form to internal contact force form, we reach:

$$\begin{aligned} \langle \sigma_{ij} \rangle =& \frac{1}{V} \sum_{c \in I} f_i^c l_j^c + \frac{1}{V} \sum_{e \in E} f_i^e l_j^e \\ &+ \frac{1}{V} \sum_{p \in V} (f_i^p - w_i^p) x_j^{Gp} - \frac{1}{V} \int_V (\rho \ddot{x}_i - \gamma_i) x_j dV \end{aligned} \tag{10}$$

where $\boldsymbol{f}^p$ denotes the resultant force on particle 'p' centroid, and $\boldsymbol{w}^p$ the gravity force vector of particle 'p' acting at $\boldsymbol{x}^{Gp}$.

8

Note the 2nd term in Eq.(10),

$$\frac{1}{V} \sum_{e \in E} f_i^e l_j^e,$$

stems exactly from the 2nd term (*boundary-radius-gap* term) in Eq.(9),

$$\frac{1}{V} \sum_{p \in \partial V} f_i^{ext,p} r_j^p,$$

where l_j^e is the branch vector to the boundary point e, defined in Bagi (1999, 2003).

As a result, Eq.(5) becomes

$$
\begin{aligned}
\langle \sigma_{ij} \rangle_{Nicot-2} =& \frac{1}{V} \left(\sum_{c \in I} f_i^c l_j^c + \sum_{e \in E} f_i^e l_j^e \right) \\
& - \frac{1}{V} \sum_{p \in V} \left(\varepsilon_{ikl} \dot{\Omega}_k^p \chi_{jl}^p + \Omega_i^p \Omega_k^p \chi_{jk}^p - (\Omega^p)^2 \chi_{ij}^p \right),
\end{aligned}
\tag{11}
$$

which we call *modified Nicot's formula*.

It is clear that Eq.(11) is equivalent to Eq.(3) in static equilibrium conditions for the particles in 3D DEM. Namely, the static part of modified Nicot's formula (11) is just Bagi's formula, not Weber's formula (which does not contain the *boundary-radius-gap* term). In a dynamic simulation that eventually reaches static equilibrium, the inertial terms vanish so that Nicot's and Bagi's formulas give the same stress state.

In addition, the following equation holds in static equilibrium following the derivation, and serves as an analogy to Eq.(18) in Nicot et al. (2013):

$$
\begin{aligned}
\langle \sigma_{ij} \rangle =& \frac{1}{V} \sum_{p \in \partial V} f_i^{ext,p} x_j^{Gp} + \frac{1}{V} \sum_{p \in V} w_i^p x_j^{Gp} \\
=& \frac{1}{V} \sum_{c \in I} f_i^c l_j^c + \frac{1}{V} \sum_{e \in E} f_i^e l_j^e
\end{aligned}
\tag{12}
$$

Equation (12) reveals an important mechanical interpretation on the stress tensor of a particle assembly or RVE which is subjected to boundary forces and gravity forces in static equilibrium: the stress tensor should

9

be calculated via Bagi's formula, not Weber's formula. We call it *equation of stress equivalence.* It is proved later that the averaged stress tensor calculated from equation of stress equivalence exhibits symmetry.

Thirdly, the De Saxcé's formula, Eq.(4), should be modified as well in terms of Eq.(12). Note Eq.(7) in De Saxcé et al. (2004) is essentially the same as Eq.(7) in this paper, so Eq.(4) becomes

$$\langle \sigma_{ij} \rangle_{\text{De Saxcé}-2} = \frac{1}{V} \left(\sum_{c \in I} f_i^c l_j^c + \sum_{e \in E} f_i^e l_j^e \right) - \frac{1}{V} \left(\int_V x_i \rho a_j dV \right) \tag{13}$$

where the gravity term vanishes. We call it *modified De Saxcé's formula.* It is seen that the static part of modified De Saxcé's formula is exactly Bagi's formula.

4. ON THE SYMMETRY OF STRESS TENSORS

4.1. In classical continuum

In classical continuum mechanics (CCM), the balance of linear momentum and angular momentum for a continuum are expressed in Eq.(14) and Eq.(15), respectively.

$$\int_{\partial V} \boldsymbol{t} dS + \int_V \boldsymbol{f} dV = \boldsymbol{0}, \tag{14}$$

$$\int_{\partial V} \boldsymbol{x} \times \boldsymbol{t} dS + \int_V \boldsymbol{x} \times \boldsymbol{f} dV = \boldsymbol{0}, \tag{15}$$

$$\boldsymbol{\sigma n} = \boldsymbol{t} \text{ or } \sigma_{ij} n_j = t_i \tag{16}$$

where $\boldsymbol{x}$ denotes current coordinate in V or on ∂V, and $\boldsymbol{f}$ body force per unit volume, $\boldsymbol{f} = \rho(\boldsymbol{g} - \boldsymbol{a})$, including both gravity acceleration $\boldsymbol{g}$ and inertial acceleration $\boldsymbol{a}$, and $\boldsymbol{t}$ the traction on ∂V. Equation (16) represents Cauchy's stress theorem and gives the definition of Cauchy's stress tensor in a continuous body.

It is well known that on the basis of Eq.(16), $\sigma_{ij} = \sigma_{ji}$ if Eq.(14) and (15) are satisfied simultaneously; $\sigma_{ij} \neq \sigma_{ji}$ if Eq.(15) is not satisfied (typically because of the existence of external moment or imbalance of angular momentum, which may occur in DEM RVEs, and also in micropolar continuum mechanics). This property holds for both static and dynamic conditions pointwise in classical continuum mechanics. That is,

$$\sigma_{ij} = \sigma_{ji} \Leftrightarrow \text{balance of angular momentum} \tag{17}$$

Equation (17) implies that there is no stress couple or local rotational acceleration in the body of classical continuum mechanics (CCM), whereas they exist in micropolar continuum mechanics. In essence, the balance of angular momentum of an infinitesimally small element within a classical continuum ensures that there exists no "external" or unbalanced moment on that element.

It must be emphasized that the premise of the above equations is that the body is continuous, namely, $\boldsymbol{f}$ and $\boldsymbol{t}$ are continuous vector fields. Moreover, divergence theorem is used in the proof, which requires that volume V is compact and has a piecewise smooth boundary ∂V, and that the vector fields are continuously differentiable.

4.2. In granular media

In granular media and their numerical modeling using the Discrete Element Method (DEM), each particle satisfies the balance of linear momentum and angular momentum, therefore the overall particle assembly or RVE satisfies the balance of linear momentum and angular momentum simultaneously. Hence, the Cauchy stress tensor calculated for the particle assembly or RVE should be symmetric. De Saxcé et al. (2004) proved Cauchy stress tensor symmetry in terms of De Saxcé's formula utilizing the equations of balance of linear and angular momenta. Note the modified De Saxcé's formula is reduced to Bagi's formula for static equilibrium, so the proof of Cauchy stress symmetry in terms of Bagi's formula is incorporated as well. The proof is briefly summarized below.

The balance of linear and angular momenta are expressed in index notation as,

$$\int_{\partial V} t_i dS + \int_V f_i dV = 0, \tag{18}$$

$$\int_{\partial V} (x_i t_j - x_j t_i) dS + \int_V (x_i f_j - x_j f_i) dV = 0, \ i \neq j, \tag{19}$$

and the averaged stress is defined as

$$\langle \sigma_{ij} \rangle = \frac{1}{V} \left(\int_{\partial V} x_i t_j dS + \int_V x_i f_j dV \right). \tag{20}$$

11

Then

$$\langle\sigma_{ij}\rangle - \langle\sigma_{ji}\rangle = \frac{1}{V}\left(\int_{\partial V}(x_i t_j - x_j t_i)dS + \int_V (x_i f_j - x_j f_i)dV\right)$$

$$= 0.$$

(21)

Obviously, the symmetry of averaged stress tensor relies on the validity of balance of angular momentum of the particle assembly, in this case via DEM simulations. Equations (15) and (19) can be rewritten as follows, respectively:

$$\int_V \boldsymbol{x} \times \boldsymbol{f} dV = -\int_{\partial V} \boldsymbol{x} \times \boldsymbol{t} dS,$$

(22)

$$\int_V (x_i f_j - x_j f_i)dV = -\int_{\partial V}(x_i t_j - x_j t_i)dS,\ i \neq j.$$

(23)

For granular media, the LHS (internal or volume moment) and RHS (external or boundary moment) of Eq.(23) can be computed and compared in DEM simulations: if they are equal, then the stress tensor should be symmetric, otherwise the stress tensor is asymmetric. There are various factors that affect the equality of Eq.(23).

It is important to realize that this proof of granular media differs from that of classical continuum mechanics (CCM): $\boldsymbol{f}$ and $\boldsymbol{t}$ are not necessarily continuous vector fields; and neither Cauchy's stress theorem nor divergence theorem is required or obeyed. In granular media, there exist gaps between particles or RVEs, and one particle may move between two other particles that are previously in contact. Moreover, two particles could overlap to a certain extent numerically in DEM simulations. We make this point because the underlying physics and mathematics between continuous CCM and discrete granular mechanics are different even though the equations look alike.

To evaluate the asymmetry of the stress tensor, we define a quantity, *relative asymmetry index* (RAI), as the ratio of L^2-norm of the skew-symmetric matrix to that of the symmetric matrix with diagonal elements set to zero:

$$RAI = \frac{\left(\frac{1}{2}\left(\langle\sigma_{ij}\rangle - \langle\sigma_{ij}\rangle^T\right)\right)^{L^2-norm}}{\left(\frac{1}{2}\left(\langle\sigma_{ij}\rangle + \langle\sigma_{ij}\rangle^T\right)\right)^{L^2-norm}_{diag=0}}$$

(24)

12

The RAI serves as an estimate of relative deviation of the averaged stress tensor from a symmetric tensor. It only involves non-diagonal elements of the stress tensor matrix according to Eq.(24). As shown in later sections, various stress tensor matrices are calculated and reported, and corresponding RAIs are listed to reveal the relative asymmetry.

In terms of Eq.(21), we define absolute asymmetry (AA) as

$$AA = \left(\langle \sigma_{ij} \rangle - \langle \sigma_{ji} \rangle \right)^{L^2-norm} \tag{25}$$

4.3. Other factors

When the particles form a "continuous" state, the stress definition is valid and satisfies symmetry. However, there are other factors that may influence the calculation of stress tensor and its symmetry in a DEM simulation system.

4.3.1. Damping mechanism

A particle in a granular assembly is subjected to contact forces, gravity, boundary force, and damping forces. For each particle the equation of motion can be expressed as

$$\boldsymbol{Ma} + \boldsymbol{Cv} + \boldsymbol{P} = \boldsymbol{F} \tag{26}$$

where $\boldsymbol{a}$ denotes generalized acceleration, $\boldsymbol{v}$ generalized velocity, $\boldsymbol{M}$ generalized mass matrix, $\boldsymbol{C}$ generalized global damping matrix, $\boldsymbol{P}$ generalized contact force, and $\boldsymbol{F}$ generalized external force. For example,

$$\boldsymbol{M} = \begin{bmatrix} m & 0 & 0 & 0 & 0 & 0 \\ 0 & m & 0 & 0 & 0 & 0 \\ 0 & 0 & m & 0 & 0 & 0 \\ 0 & 0 & 0 & I_x & 0 & 0 \\ 0 & 0 & 0 & 0 & I_y & 0 \\ 0 & 0 & 0 & 0 & 0 & I_z \end{bmatrix} \tag{27}$$

$$\boldsymbol{C} = \alpha \boldsymbol{M} \tag{28}$$

where m denotes mass, I moment of inertia, and α coefficient of global damping.

The equation of motion (26) is integrated in time using central difference method for its simplicity and second order accuracy, and the following midstep velocity is obtained as

$$\boldsymbol{v}_{n+1/2} = \frac{1 - \alpha \Delta t/2}{1 + \alpha \Delta t/2} \boldsymbol{v}_{n-1/2} + \frac{1}{1 + \alpha \Delta t/2} \Delta t \boldsymbol{M}^{-1} [\boldsymbol{F}_n - \boldsymbol{P}_n] \tag{29}$$

where n denotes the nth time, and Δt is the time step. Equation (29) can be evaluated at any time n to obtain the midstep generalized velocity $\boldsymbol{v}_{n+1/2}$, and then the generalized displacement (including translation and rotation).

A dynamic relaxation (DR) procedure (Key et al., 1980; Underwood, 1983) is often performed in quasi-static DEM simulations, whereby only $\boldsymbol{P}$ and $\boldsymbol{F}$ must represent the physical forces and moments, while $\boldsymbol{C}$ and $\boldsymbol{M}$ are fictitious values such that the static solution is obtained using a minimum number of steps.

The generalized global damping $\boldsymbol{C} = \alpha \boldsymbol{M}$ is also referred to as background damping, which is sometimes necessary to apply to individual particles to dissipate their energy. Aside from that, interparticle contact damping is essential and physical to model the mechanical interaction between particles. The contact interface is illustrated in Fig.2, characterized by normal stiffness k_n, tangential stiffness k_t, friction coefficient μ, and normal contact damping coefficient c_n. The interparticle damping mechanism is incorporated in the term $\boldsymbol{P}$, the generalized contact force, depending on the specific damping model.
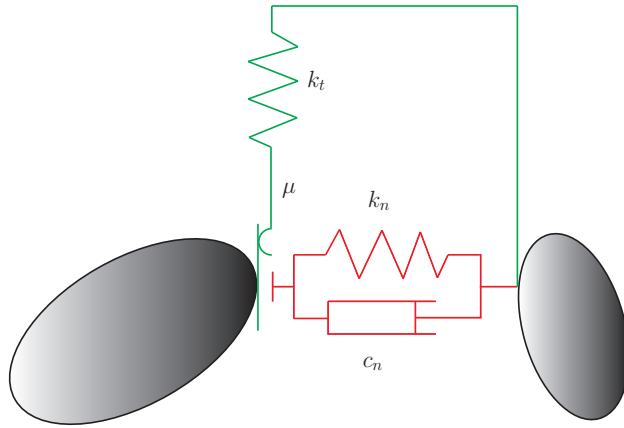

Figure 2: Model of contact interface.

Both damping mechanisms may be applied in a DEM simulation system. The global damping is usually applied to each individual particle and unavoidably affects the linear and angular momenta of the particle; the interparticle contact damping is applied to each pair of in-contact particles as a pair of action and reaction "force," which has no bearing on the linear momentum, yet may have slight influence on angular momentum of the particle

14

assembly. Obviously, the stress tensor formulas presented in this paper do not take this into account. As a result, dynamic and quasi-static simulations may demonstrate asymmetric or slightly asymmetric stress tensors because of a chosen damping mechanism.

The effect of damping can hardly be eliminated, because doing so may make the DEM simulation system unstable or unable to dissipate energy when friction is not present. Static simulations or static equilibrium state obtained by dynamic simulations do not have this problem, because the damping mechanism normally vanishes at the instant of reaching static equilibrium.

4.3.2. Stress wave propagation effect

Something more important than the damping mechanisms in affecting stress calculation is the *stress wave effect*. In dynamic simulations, forces exerted on the boundary of the particle assembly in each time step are not perceived instantaneously by the interior of the particle assembly, because it takes a certain number of time steps for the DEM system to transmit boundary forces. No doubt this also holds true for quasi-static simulations to a certain degree. When the stress wave effect is pronounced, the balance of linear and angular momenta in DEM are not satisfied at an instant of discrete time, namely, Eq.(23) does not hold, and the stress tensor is asymmetric.

To put it simpler, when a dynamic boundary condition (force condition, displacement condition, or a combination) is applied to a particle assembly, it actually exerts an external moment, or more accurately, an imbalance of angular momentum, to the particle assembly, and the particle assembly undergoes an overall "rotational" acceleration, or so called "intrinsic spin." This phenomenon does not exist in an infinitesimally small element within a continuous body of CCM, for which it always holds $\sigma_{ij} = \sigma_{ji}$ pointwise, since it assumes that the balance of angular momentum is always satisfied at a material point (or infinitesimal differential volume); namely, there are no stress couples or local rotational accelerations.

The overall "rotation" or intrinsic spin of a particle assembly may not be intuitive; for example, it even exists during oedometer/uniaxial compressions in which the specimen only undergoes axial strain. Actually, any form of deformation of granular media implies or includes independent rotation, which is an essential difference from classical continuum mechanics (CCM). How to define the rotation and associate it to stress may need micropolar continuum theory and goes beyond the scope of this work, but clearly the overall

rotation is related to the rotation of each individual particle: at the coarsest scale the particle assembly rotates (CCM misses); at the finest scale each particle rotates (CCM misses); and in-between scales exist, which consist of clusters of particles that undergo rotation as well (CCM misses).

Lin et al. (2015) used a micropolar hypoplastic framework (including a characteristic length as a regularization parameter) to capture the development and propagation of a persistent shear band in a rectangular specimen of silicaconcrete sand with spatially varying density. The results showed that FEM mesh sizes associated with different internal length parameters (1x, 2x and 4x of the mean grain diameter of the sand sample) produced nearly the same load-compression responses.

Lin and Wu (2016) showed that the stress asymmetry depends on the size of the averaging volume, which can be linked to the characteristic length scale in continuum models. They pointed out: "If the characteristic length is much larger than the mean particle diameter, the stress averaging volume is also very large so that the stress asymmetry can be neglected. However, if a length scale equivalent to the particle scale is used, the stress asymmetry becomes significant comparing to other stress component. Therefore, asymmetric stress tensors should be used to obtain enhanced continuum model to describe scale dependent phenomena."

Omidvar et al. (2012) pointed out that stress is non-uniform in high-strain-rate oedometer/uniaxial compression, and two approaches have been used to overcome the problem in stress measurement: (1) reduce the thickness of the sample, and (2) allow stress wave to propagate and reflect many times before the impact stress is fully applied to the specimen. However, DEM has the advantage to capture the whole process of stress wave propagation in granular media at any instant in time.

5. NUMERICAL INSPECTION USING DEM

In this section, numerical simulations are performed using a DEM code, ParaEllip3d (Yan, 2008; Yan et al., 2010; Yan and Regueiro, 2018a,b), to verify the stress tensor and its symmetry. ParaEllip3d is a 3D DEM code developed at the University of Colorado Boulder with general capacity to simulate a wide range of laboratory experiments and in-situ field tests that involve a large number of complex-shaped grains or particles. The interparticle contact mechanism is based on the nonlinear Hertzian normal contact model and history-dependent Mindlin's shear contact model, combined with

Coulomb friction and interparticle contact damping. The simulated particle shapes range from spherical to three-axis ellipsoidal (with variation of 1st and 2nd aspect ratios), to non-axisymmetric ploy-ellipsoidal (with variation of 1st and 2nd aspect ratio, and variation of three non-axisymmetry ratios). It is capable of modeling particulate assemblies that are composed of up to 10 million complex-shaped grains or CPU-demand equivalent to 1 billion spheres. The simulation types include but are not limited to: grain number/size/mass distribution and filtering; gravitational deposition (pluviation or raining); degravitation response; isotropic compression; oedometer/uniaxial compression; conventional triaxial compression; true triaxial compression; plane-strain compression; quasi-static and dynamic penetration; high-strain-rate impact and deformation; compressive and shear wave propagation; constrained and unconstrained collapse; hierarchical multiscale coupling with Finite Element Method (FEM); two-way multiphysics coupling with Computational Fluid Dynamics (CFD) for shock wave or explosive wave interaction, etc.

5.1. A simple 2D case

A simple 2D case is studied using dynamic DEM simulation: a 10x10 horizontal sphere matrix is isotropically compressed in horizontal direction by applying a constant inward force (0.05 N) on each boundary sphere. The radius of each particle is 5 mm, and particles are weightless and frictionless. Interparticle contact damping is adopted for the system to achieve static equilibrium. Figure 3 plots the spatial distribution, energy process and final state of the contact forces between particles for this particulate system. Note the contact forces are plotted using unarrowed vectors for which the line segment centers coincide with the contact points between particles.

Then a matrix of 181 large and small spheres is tested, as shown in Fig.4. The small particles have the exact size to fit in the void space between large particles before compression, with centroids located at the same horizontal level.

Lastly, 9 randomly-selected small particles are removed, and the remaining 172 particles are tested, as shown in Fig.5.
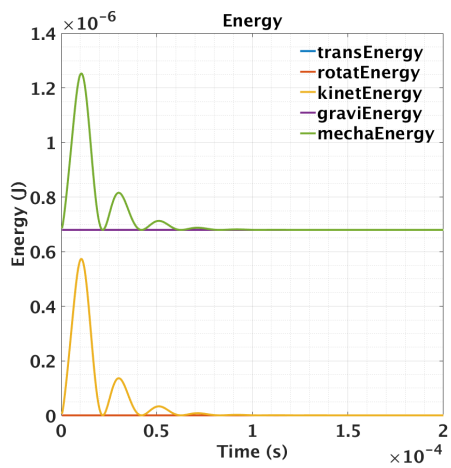
Table 1 lists the 3x3 matrix of stress tensors calculated from the three tests. Note the stresses in this paper use sign convention of solid mechanics (tension positive and compression negative). It is seen that the shear stresses do not exist in cases 1 and 2. The non-zero small values of shear stress are
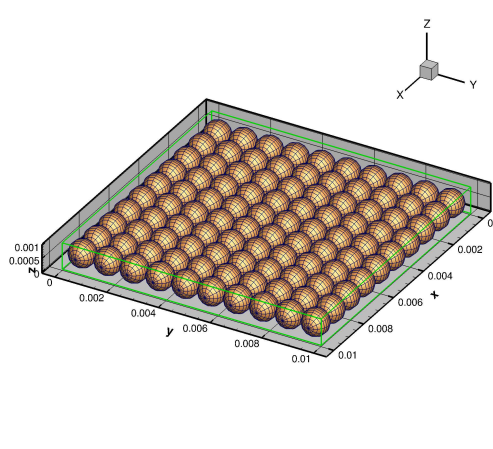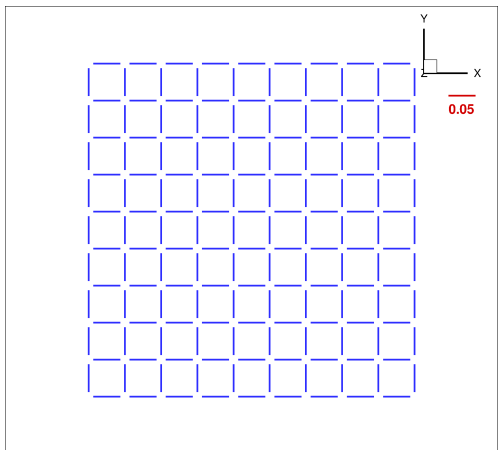
(a) 3D view
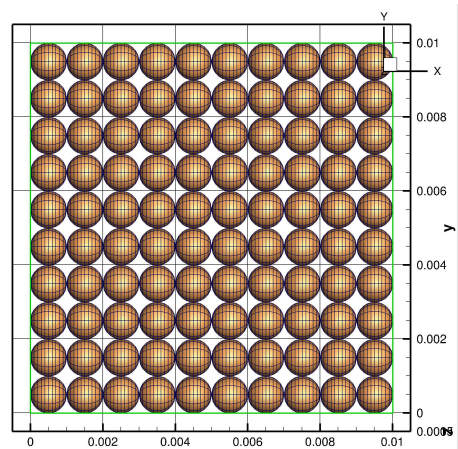
(b) Top view

(c) Energy process

(d) Contact forces

Figure 3: Isotropic compression of 100 spheres.

18

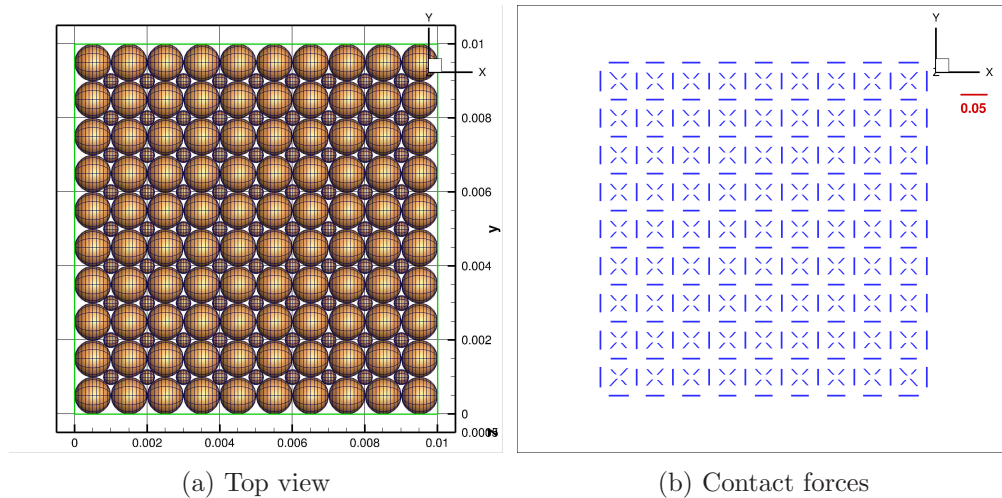(a) Top view   (b) Contact forces

Figure 4: Isotropic compression of 181 spheres.

due to the limitation of numerical precision. In case 2, the oblique contact forces between large and small particles are canceled out in stress calculation.

However, the oblique contact forces in case 3 are not canceled out and result in a shear component in the stress tensor, due to the random voids created by removal of 9 small particles, which is clearly observed from the zoomed-in contact force distribution shown in Fig.5(c,d). Actually, the final state of the 172 particle system is not exactly in 2D isotropic compression because the boundary particles have moved non-uniformly. Through this simple case we show how shear stress is generated in this frictionless system. It is anticipated that shear components exist in an assembly composed of particles with a variety of size, shape, gradation and spatial distribution.

The stress tensor with non-zero shear stress for case 3 (172 particles) exhibits symmetry, which agrees with Bardet and Vardoulakis (2001)'s statement: "the computed asymmetry of stress tensor in statics implies inaccurate calculation and/or lack of static equilibrium."

The stress tensor calculated from cases 1 and 2 are the same, namely, the stress tensor is not affected by the "density" of the particle system. If even smaller particles are used to fill in the remaining space in case 2 regularly, the stress tensor will remain the same. The stress is objective and independent of density of the particulate system.
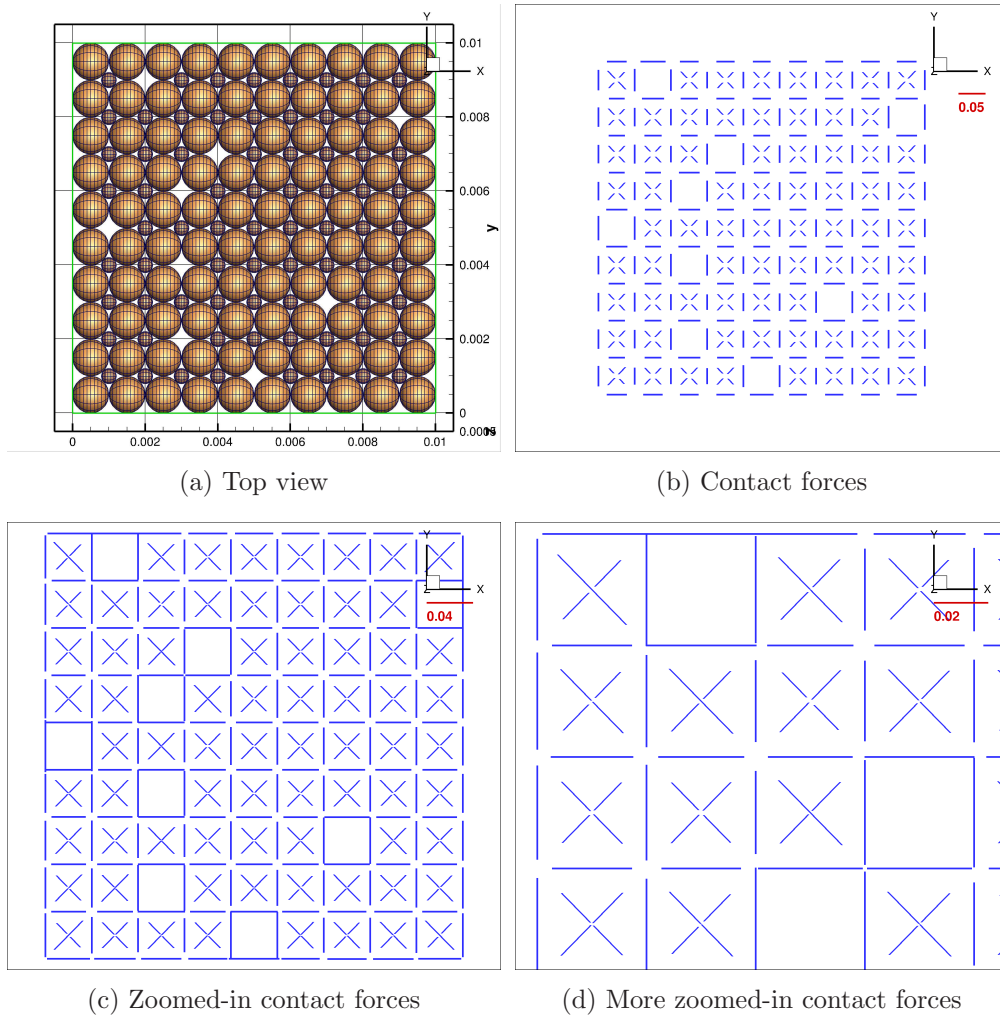
(a) Top view

(b) Contact forces

(c) Zoomed-in contact forces

(d) More zoomed-in contact forces

Figure 5: Nearly isotropic compression of 172 spheres.

20

Table 1: Stress tensor of 2D compression

particles	stress tensor		
100	-5.00E+04	1.96E-08	-2.84E-21
	1.96E-08	-5.00E+04	-2.84E-21
	-2.84E-21	-2.84E-21	4.60E-23
181	-5.00E+04	4.01E-08	-1.43E-21
	4.01E-08	-5.00E+04	-1.48E-21
	-1.48E-21	-1.43E-21	1.89E-23
172	-5.00E+04	-6.52E+00	2.02E-15
	-6.52E+00	-5.00E+04	1.94E-15
	-8.34E-17	2.02E-15	1.27E-21

5.2. Static state from gravitational deposition

In this test, the particles are initially "floated" in space without interaction and then gravitationally deposited into a rigid container. At the end, all particles come to rest and are packed under gravity. The parameters are listed in Table 2. Note that all simulations in this paper only use interparticle damping, and do not apply any global damping in order to eliminate the influence of damping "force" on the linear and angular momenta of the particle assembly in dynamic or quasi-static state.

Young's modulus E (Pa)	4.5×10^{10}
Poisson's ratio ν	0.25
specific gravity G_s	2.65
interparticle coef. of friction μ	0.5
particle-wall coef. of friction μ_2	0.5
interparticle contact damping ratio ξ	0.85
particle radii (m)	$0.001 \sim 0.0025$
particle shape (aspect ratio)	1:1:1 or 1:0.8:0.6
time step $\triangle t$ (sec)	5.0×10^{-7}

Table 2: Numerical parameters used in DEM pluviation simulation.

5.2.1. Monodisperse spherical particle assemblies

Firstly, monodisperse spherical particle assemblies (1.5 mm radius) are tested with different number of particles: 68, 153, 600, 1,176, 1,536, 2,400 and 3,456, respectively. The final rested state for each of these particle assemblies are illustrated in Fig.6. The processes of boundary contact forces and assembly energy for 68 and 3,456 particles are plotted in Fig.7, and it is observed that the rotational energy takes a very small fraction relative to the translational energy during the process of particle packing and rebounding.
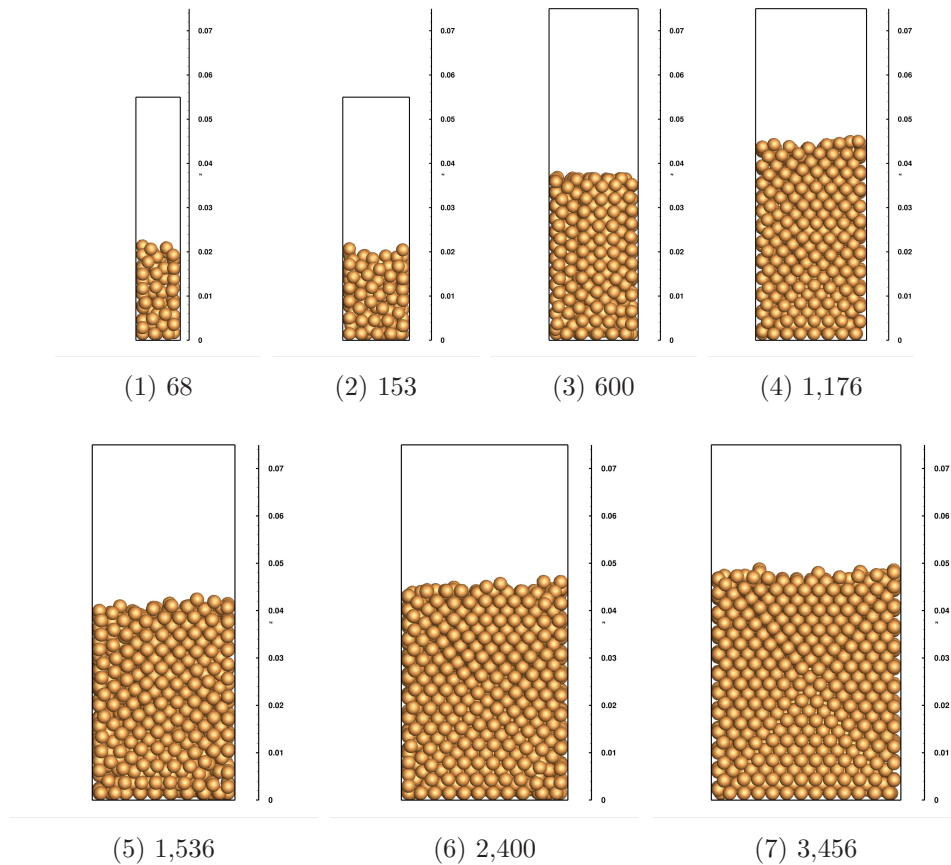

Figure 6: Rested state of monodisperse spherical particle assemblies.

Table 3 lists the 3x3 matrix of stress tensors calculated by Weber's and Bagi's formulas for the 7 cases. It is clear that the stress tensor by Weber's formula is asymmetric for small number of particles, and the asymmetry decreases with an increasing number of particles; whereas stress tensor by

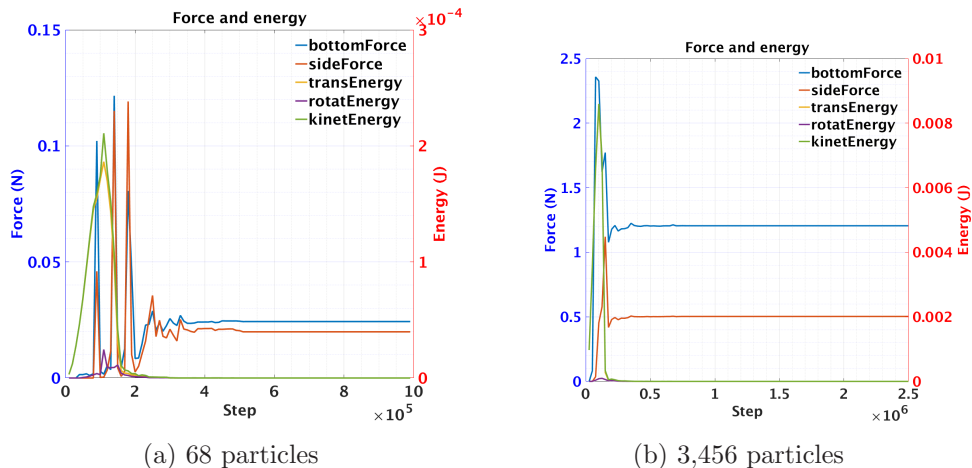(a) 68 particles   (b) 3,456 particles

Figure 7: Boundary contact forces and assembly energy in gravitational deposition.

Bagi's formula exhibits excellent symmetry from 68 particles to 3,456 particles. Even at the level of 3,456 particles, the stress gap between Weber's and Bagi's formulas is still apparent.

The RAI's are calculated for all cases. By Weber's formula, it is as high as 15.1% for 68 particles and as low as 1.1% for 1,176 particles, while it is below 0.03% by Bagi's formula. As a technical index, the RAI value of 1% indicates clear asymmetry, and 5% represents strong asymmetry. A stress tensor matrix with RAI below 0.03% may be regarded as symmetric.

When the number of particles becomes sufficiently large, Weber's formula may or may not generate a very close result to Bagi's formula, depending on particle size gradation and spatial distribution. Its stress symmetry cannot be proved, while Bagi's formula guarantees stress tensor symmetry, as proved in Section 4.

In numerical simulations to study particulate systems, it is challenging to use sufficiently large number of particles. As an estimate, modern supercomputers are typically capable of computing up to $15,000 \sim 30,000$ particles per core (PPC) of spheres, and $150 \sim 300$ PPC of complex-shaped particles such as ellipsoid or poly-ellipsoid with optimal computational granularity (CG) for large-scale MPI simulations (Yan and Regueiro, 2018a).

5.2.2. Polydisperse ellipsoidal particle assemblies

Secondly, polydisperse ellipsoidal particle assemblies (1.0 to 2.5 mm radius) are tested with different number of particles: 69, 179, 476, 1,071, 1,904

Table 3: Static stress tensor of monodisperse spherical particle assemblies.

particles	Weber's formula			RAI (%)	Bagi's formula			RAI (%)
	stress tensor				stress tensor			
68	-6.44E+01	-1.15E+01	-2.72E+00		-9.07E+01	-9.70E+00	-1.19E+00	
	-8.11E+00	-6.16E+01	-5.34E+00	15.1	-9.70E+00	-8.76E+01	-4.44E+00	8.03E-05
	-1.37E+00	-5.50E+00	-1.09E+02		-1.19E+00	-4.44E+00	-1.25E+02	
153	-8.12E+01	-2.31E-01	2.55E+00		-1.01E+02	4.87E-01	2.82E+00	
	-1.35E-04	-7.86E+01	-8.39E+00	2.2	4.87E-01	-9.84E+01	-9.15E+00	2.33E-03
	2.54E+00	-8.09E+00	-9.68E+01		2.82E+00	-9.15E+00	-1.15E+02	
600	-1.46E+02	-2.85E+01	8.86E+00		-1.71E+02	-2.83E+01	7.75E+00	
	-2.72E+01	-1.51E+02	1.48E+01	2.2	-2.83E+01	-1.76E+02	1.50E+01	5.29E-05
	9.21E+01	1.56E+01	-2.54E+02		7.75E+00	1.50E+01	-2.80E+02	
1,176	-2.35E+02	3.97E+01	-8.45E+00		-2.66E+02	3.95E+01	-8.25E+00	
	3.96E+01	-2.34E+02	-1.42E+01	1.1	3.95E+01	-2.65E+02	-1.39E+01	1.74E-05
	-7.88E+00	-1.34E+01	-3.05E+02		-8.25E+00	-1.39E+01	-3.27E+02	
1,536	-1.88E+02	-9.42E+00	4.69E+00		-2.09E+02	-9.84E+00	5.25E+00	
	-9.95E+00	-1.90E+02	-1.05E+00	5.2	-9.84E+00	-2.11E+02	-4.00E-01	2.71E-02
	5.62E+00	-5.35E-01	-2.55E+02		5.25E+00	-4.00E-01	-2.76E+02	
2,400	-2.42E+02	-3.77E+00	-8.39E+00		-2.65E+02	-3.84E+00	-8.16E+00	
	-4.24E+00	-2.43E+02	2.18E+00	4.0	-3.84E+00	-2.66E+02	2.56E+00	2.94E-04
	-8.16E+00	2.81E+00	-3.32E+02		-8.16E+00	2.56E+00	-3.55E+02	
3,456	-2.29E+02	1.11E+01	-2.17E+00		-2.47E+02	1.10E+01	-1.98E+00	
	1.14E+01	-2.29E+02	-1.89E+00	1.7	1.10E+01	-2.48E+02	-1.64E+00	2.07E-03
	-2.07E+00	-1.57E+00	-3.56E+02		-1.98E+00	-1.64E+00	-3.79E+02	

and 2,975 respectively. The final rested state of these particle assemblies are illustrated in Fig.8.

Table 4 lists the 3x3 matrix of stress tensors calculated by Weber's and Bagi's formulas for the 6 cases. It exhibits a trend similar to that of monodisperse spherical particle assemblies. The stress from Bagi's formula exhibits excellent symmetry when the number of particles goes beyond 179 in these tests. It is worth noting that the contact geometry resolution between ellipsoids is numerically challenging. Yan et al. (2010) developed a robust contact resolution algorithm for three-axis ellipsoidal particles by constructing an *extreme value problem* of finding the deepest penetration of one particle into the other. Such an extreme value problem results in a sixth order polynomial equation. Conventional polynomial root finders cannot satisfy the high-precision numerical requirement in the 3D DEM computation. For example, the elastic overlap between two particles of typical quartz sand may vary between 10^{-8} to 10^{-5} meters depending on particle size, shape and external force, and a low-precision solver can lead to numerical instability or spurious explosion of particles. Therefore, an iterative eigenvalue method is selected to find roots of the polynomial and determine the contact geometry. The algorithm and its implementation has been shown to be robust such that it is applicable to not only regularly bulky ellipsoidal shapes but also
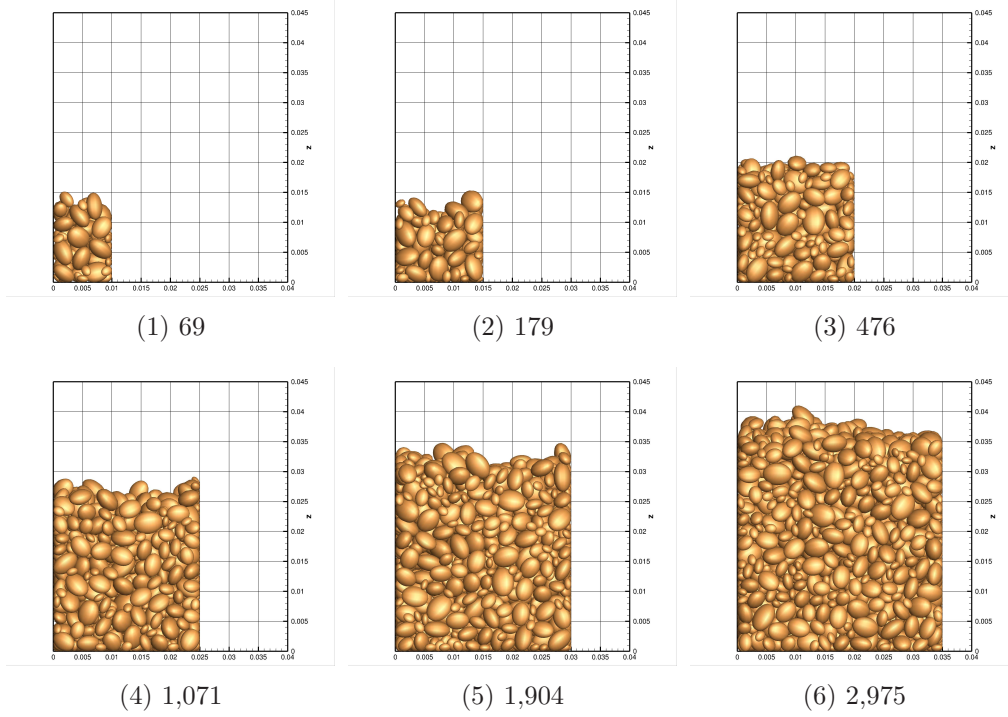
Figure 8: Rested state of polydisperse ellipsoidal particle assemblies.

Table 4: Static stress tensor of polydisperse ellipsoidal particle assemblies.

particles	Weber's formula				Bagi's formula			
	stress tensor			RAI (%)	stress tensor			RAI (%)
69	-2.83E+01	1.76E+00	9.77E-02		-4.12E+01	-5.52E-01	1.77E+00	
	1.39E+00	-3.77E+01	1.30E+01	3.9	-6.30E-01	-5.75E+01	1.57E+01	2.80E-01
	-3.45E-01	1.39E+01	-6.30E+01		1.74E+00	1.57E+01	-8.10E+01	
179	-4.62E+01	5.09E-01	3.03E-01		-5.81E+01	7.73E-01	9.67E-01	
	1.44E+00	-4.10E+01	2.27E+00	30.0	7.73E-01	-5.09E+01	8.39E-01	2.47E-03
	-4.20E-01	1.66E+00	-5.61E+01		9.67E-01	8.39E-01	-6.98E+01	
476	-8.36E+01	5.66E+00	1.58E+00		-9.81E+01	3.67E+00	1.57E+00	
	3.58E+00	-8.39E+01	2.35E+00	20.3	3.67E+00	-9.74E+01	2.62E+00	3.29E-03
	1.90E+00	3.94E+00	-1.09E+02		1.57E+00	2.62E+00	-1.26E+02	
1,071	-1.19E+02	7.53E+00	2.66E+00		-1.36E+02	8.36E+00	3.67E+00	
	6.95E+00	-1.18E+02	3.81E+00	6.3	8.36E+00	-1.33E+02	-3.01E-01	9.05E-03
	3.41E+00	7.62E-01	-1.51E+02		3.68E+00	-3.00E-01	-1.66E+02	
1,904	-1.32E+02	-2.81E+00	8.30E+00		-1.47E+02	-1.49E+00	9.85E+00	
	-2.27E+00	-1.29E+02	-7.09E-02	4.8	-1.49E+00	-1.43E+02	-8.66E-01	2.23E-02
	8.36E+00	-7.34E-01	-1.79E+02		9.85E+00	-8.62E-01	-1.96E+02	
2,975	-1.60E+02	1.49E+00	-5.74E-01		-1.75E+02	1.25E+00	5.09E-01	
	1.09E+00	-1.71E+02	3.43E+00	6.3	1.24E+00	-1.85E+02	4.35E+00	2.37E-02
	-1.00E-01	3.80E+00	-2.13E+02		5.07E-01	4.35E+00	-2.29E+02	

extreme-shaped ellipsoidal particles such as disks and needles.

The RAI by Weber's formula ranges from 3.9% to 30.0%, indicating strong asymmetry; while it is typically below 0.03% by Bagi's formula.

From the perspective of stress tensor calculation, the number of particles in the RVE does not need to large, namely, tens or hundreds of particles would be adequate provided that high-precision contact geometric resolution is assured.

Göncü and Luding (2013) studied the effect of particle ploydispersity on the macroscopic stress-strain relationship using $1 \sim 5mm$ spherical particles.

5.2.3. Cauchy's stress theorem

It is interesting to see if the averaged stress follows the Cauchy's stress theorem, which is based on the concept of an infinitesimally small element in CCM, namely, a material point. The stress tensor calculated in granular materials differs in that it is an averaged value among multiple or many individual particles in a DEM RVE.

As an example, the static stress of the assembly composed of 3,456 monodisperse spherical particles in Section 5.2.1 is inspected. Figure 9 illustrates these particles with a 3D and side view.

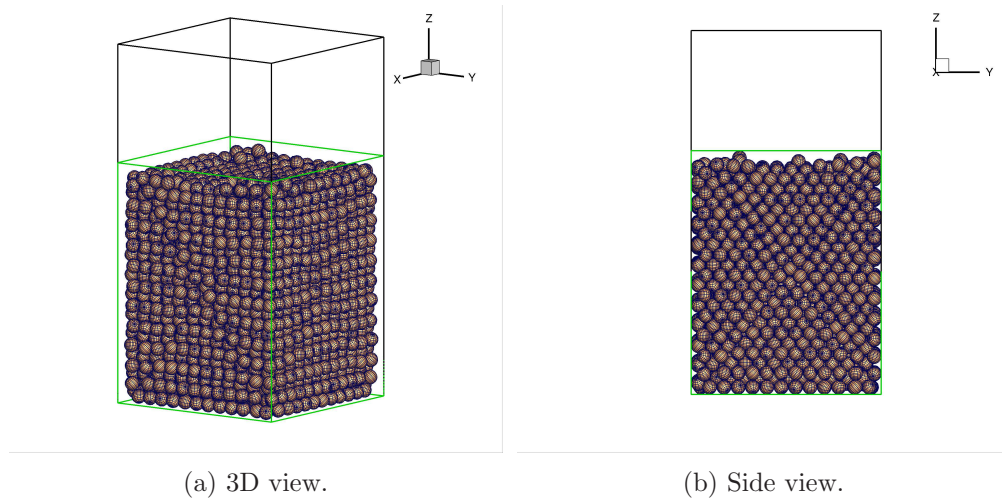(a) 3D view. (b) Side view.

Figure 9: Boundary contact force distribution of 3,456 spheres at rest.

The internal contact forces, and boundary contact forces along the five walls of the rigid container are captured in Fig.10. Note the contact forces

include both normal and tangential components, and the tangential components are much smaller than the normal ones. Clearly the boundary contact forces along the gravity direction do not exhibit a uniform distribution because it should increase with increasing depth, illustrated by Fig.10(c). In the horizontal direction shown in Fig.10(d), the contact forces are not uniformly distributed either, and the contact forces in the corners seem to be higher.
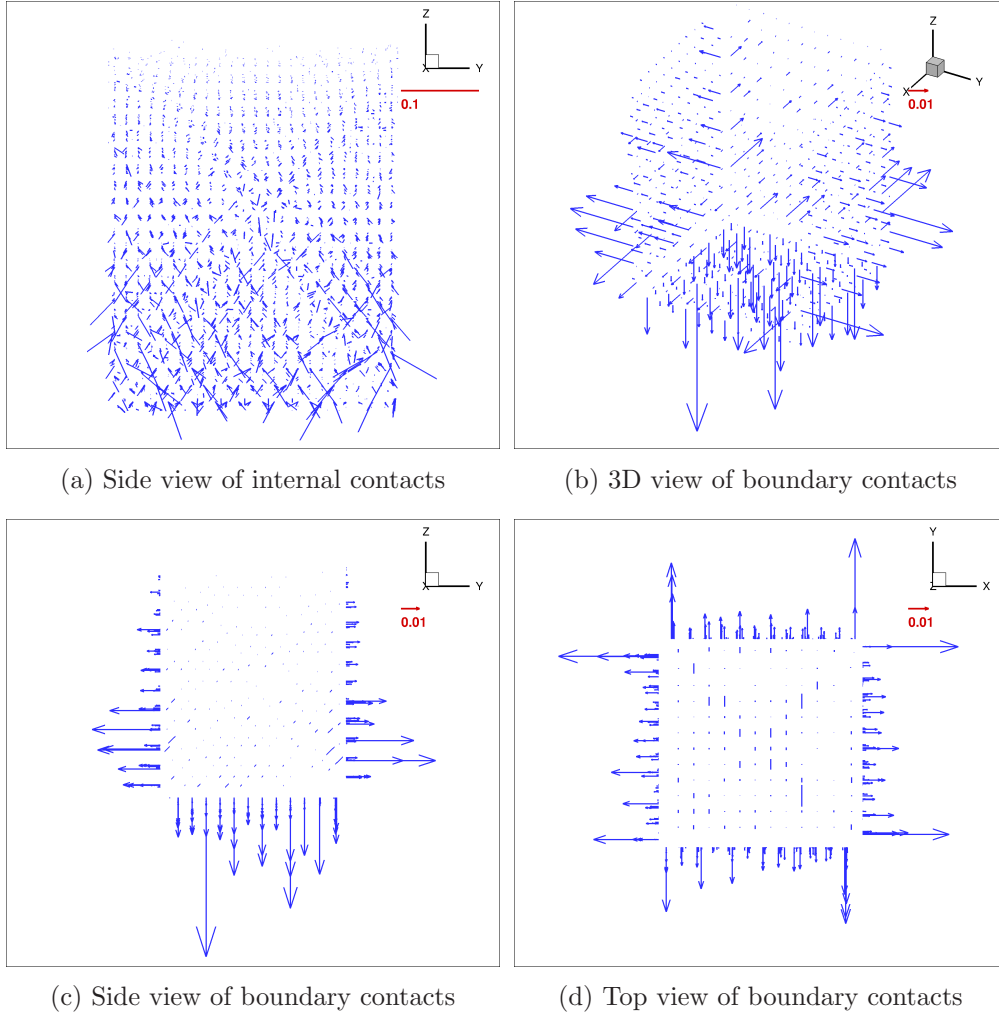

(a) Side view of internal contacts

(b) 3D view of boundary contacts

(c) Side view of boundary contacts

(d) Top view of boundary contacts

Figure 10: Boundary contact force distribution of 3,456 spheres at rest.

The tractions on the side wall in $+y$ direction and the bottom wall in $-z$ direction are calculated by summation of all of the contact forces acting on

the walls, respectively. Note that sign convention in solid mechanics is used and the unit is Pa.

$$\boldsymbol{\tau}_{+y} = \begin{bmatrix} \tau_x \\ \tau_y \\ \tau_z \end{bmatrix} = \begin{bmatrix} 8.89 \\ -242 \\ -9.73 \end{bmatrix},$$

$$\boldsymbol{\tau}_{-z} = \begin{bmatrix} \tau_x \\ \tau_y \\ \tau_z \end{bmatrix} = \begin{bmatrix} 6.49 \\ 8.52 \\ 753 \end{bmatrix}. \tag{30}$$

From Table 3, the stress tensor is

$$\boldsymbol{\sigma} = \begin{bmatrix} \sigma_{xx} & \sigma_{xy} & \sigma_{xz} \\ \sigma_{yx} & \sigma_{yy} & \sigma_{yz} \\ \sigma_{zx} & \sigma_{zy} & \sigma_{zz} \end{bmatrix}$$

$$= \begin{bmatrix} -247 & 11.0 & -1.98 \\ 11.0 & -248 & -1.64 \\ -1.98 & -1.64 & -379 \end{bmatrix}. \tag{31}$$

Clearly, in $-z$ direction,

$$[\boldsymbol{\sigma}] \begin{bmatrix} 0 \\ 0 \\ -1 \end{bmatrix} = \begin{bmatrix} 1.98 \\ 1.64 \\ 379 \end{bmatrix} \neq \begin{bmatrix} 6.49 \\ 8.52 \\ 753 \end{bmatrix}. \tag{32}$$

And in $+z$ direction the traction is nil, and the inequality holds. Averaging between $+z$ and $-z$ directions reduces the degree of inequality significantly, for example, $-\sigma_{zz} = 379 \approx (753 + 0)/2$, but the inequality still holds.

In $+y$ direction,

$$[\boldsymbol{\sigma}] \begin{bmatrix} 0 \\ 1 \\ 0 \end{bmatrix} = \begin{bmatrix} 11.0 \\ -248 \\ -1.64 \end{bmatrix} \neq \begin{bmatrix} 8.89 \\ -242 \\ -9.73 \end{bmatrix}, \tag{33}$$

where the values are closer, for example, $\sigma_{zz} = -248 \approx -242$ and shear components are different, so the inequality still exits.

Obviously, the Cauchy's stress theorem is not accurately satisfied in granular media, because the averaged stress is a quantity of volume average (not a pointwise value), and may contain gradient of stress that should not appear in the definition of stress pointwise in continuum mechanics. The averaged

28

stress tensor is more like a quantity that is obtained for a "microelement" or "microvolume" in micropolar continuum theory. The "microelement" is small enough and its motion consists of a translation, a "rotation" about its center of mass, and an affine deformation (Eringen, 1968),

5.3. Bagi's vs Weber's vs Drescher's formulas

The static stress tensor as calculated from Weber's, Drescher's and Bagi's formulas are compared in Table 5, using the assembly of 1,536 monodisperse spherical particles.

Table 5: Stress calculated from various formulas

formula	stress tensor			RAI (%)
Bagi	-2.09E+02	-9.84E+00	5.25E+00	0.028
	-9.84E+00	-2.11E+02	-4.00E-01	
	5.25E+00	-4.00E-01	-2.76E+02	
Weber	-1.88E+02	-9.42E+00	4.69E+00	5.2
	-9.95E+00	-1.90E+02	-1.05E+00	
	5.62E+00	-5.35E-01	-2.55E+02	
Drescher	-2.09E+02	-9.84E+00	5.25E+00	94.7
	-9.84E+00	-2.11E+02	-4.74E-01	
	2.19E+02	2.14E+02	1.88E+01	

Firstly, the stress calculated from Weber's and Drescher's formula are asymmetric, and they are different from the result of Bagi's formula. This helps to verify Eq.(6) in Section 3, namely, Drescher's formula is not equivalent to Bagi's formula.

Secondly, the RAI by Bagi's formula is low (below 0.03%); the RAI by Weber's formula is 5.2% and indicates strong asymmetry; the RAI by Drescher's formula is 94.7% representing high asymmetry. In addition, the σ_{zz} component by Drescher's formula seems to deviate significantly from that by Weber's and Bagi's formulas.

5.4. Quasi-static isotropic compression

The assembly of 3,456 monodisperse spherical particles is trimmed to 3,008 particles from the top, placed in a six-wall rectangular box, and then

29

applied with isotropic confining pressure that increases from 1 kPa to 100 kPa. Figure 11 displays the configurations, and the compression deformation is so small that it is hardly observed from the figures.

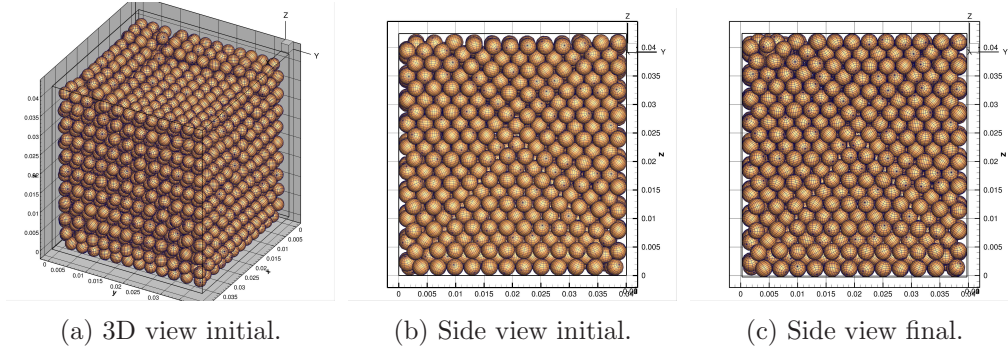(a) 3D view initial.   (b) Side view initial.   (c) Side view final.
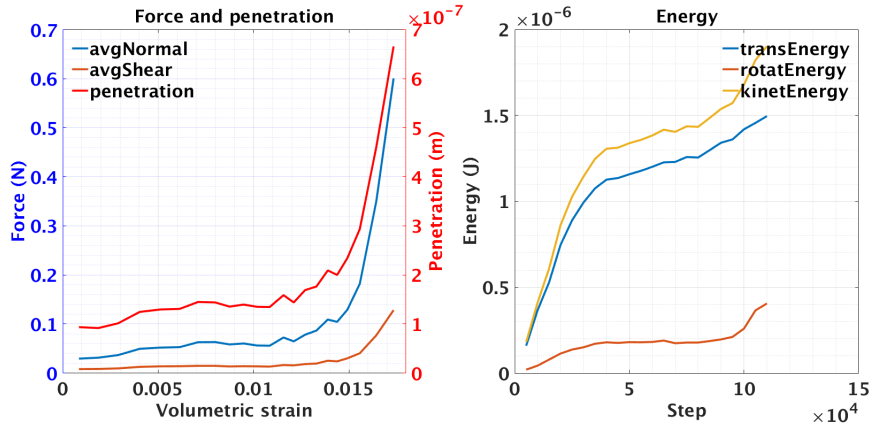
Figure 11: Isotropic compression of 3,008 spheres.

Figure 12: Force and energy in isotropic compression.

Figure 12 plots the process of contact forces and energy of the assembly: the left figure shows normal component and shear component of the average contact forces, and average overlap between particles; and the right figure shows the translational, rotational and kinetic energy (sum of the translational and rotational energy). All of these quantities increase during the

process of isotropic compression. The rotational energy is much lower than the translational energy and takes approximately 15% of the kinetic energy.

Table 6: Stress tensor calculated from isotropic compression

| formula	early stage (005) stress tensor			RAI (%)	late stage (021) stress tensor			RAI (%)
	-2.63E+03	-4.34E+02	3.06E+02		-7.68E+04	-2.00E+03	-6.49E+03	
Bagi	-4.55E+02	-2.62E+03	2.57E+02	1.8	-1.97E+03	-7.57E+04	-5.43E+03	0.3
	3.09E+02	2.45E+02	-3.58E+03		-6.49E+03	-5.39E+03	-8.27E+04	
	-2.63E+03	-4.37E+02	3.03E+02		-7.68E+04	-2.00E+03	-6.49E+03	
De Saxcé	-4.58E+02	-2.62E+03	2.53E+02	1.7	-1.97E+03	-7.57E+04	-5.43E+03	0.3
	3.08E+02	2.44E+02	-3.58E+03		-6.49E+03	-5.39E+03	-8.27E+04	
	-2.63E+03	-4.34E+02	3.03E+02		-7.68E+04	-2.00E+03	-6.52E+03	
Nicot	-4.53E+02	-2.62E+03	2.57E+02	1.5	-2.01E+03	-7.57E+04	-5.43E+03	0.2
	3.09E+02	2.54E+02	-3.58E+03		-6.49E+03	-5.43E+03	-8.27E+04	
	-2.79E+00	-2.50E+00	-3.46E+00		-5.00E-02	-4.80E-02	-6.80E-02	
De Saxcé inertia term	-2.91E+00	-2.61E+00	-3.61E+00	34.6	8.49E-01	7.60E-01	1.10E+00	56.7
	-1.21E+00	-1.08E+00	-1.49E+00		7.60E-01	6.85E-01	9.80E-01	
	3.00E-03	1.00E-04	-3.04E+00		1.00E-02	0.00E+00	-3.43E+01	
Nicot inertia term	1.44E+00	3.00E-03	-3.00E-04	95.9	-3.83E+01	1.00E-02	0.00E+00	86.7
	-2.00E-04	8.84E+00	3.00E-03		0.00E+00	-3.47E+01	1.00E-02	

Table 6 lists the 3x3 matrix of stress tensor at an early and late stage of the compression. For both stages, the Bagi stress, De Saxcé stress, Nicot stress, De Saxcé's inertial term, Nicot's inertial term are calculated, respectively. Overall, the three stress tensors (not the inertial terms) exhibit not exact but fairly acceptable symmetry. The RAI's at the early stage are $1 \sim 2\%$, and drop below 0.3% at the late stage.

The L^2-norm's of the five 3x3 matrices at the early stage are calculated: 3.80E+3, 3.79E+3, 3.80E+3, 7.7 and 8.8, respectively; and the L^2-norm's of the five 3x3 matrices at the late stage are 8.92E+4, 8.92E+4, 8.93E+4, 2.1 and 38.3, respectively. It is a bit surprising to find that the inertial terms are nearly negligible in quasi-static isotropic compression. Nicot et al. (2013) conducted a 2D numerical simulation of silo discharge using 5,250 circular disks, and the results of von Mises stress contour distribution show that the inertial terms are approximately two or more orders of magnitude smaller than that of the stress, as shown for our simulations in Table 6.

Figure 13(a) plots the volume and boundary moments, which correspond to the LHS and RHS of Eq.(23), respectively, during the process of isotropic compression. It is clear that the volume and boundary moments are not exactly the same, therefore stress asymmetry arises. Figure 13(b) shows the difference between volume and boundary moments and absolute asymmetry (AA) of stress according to Eq.(25). Overall the AA increases with the increasing moment difference. From Fig.13(c) it is observed that RAI in

terms of Eq.(24) turns out to decrease with the increasing moment difference in the process of quasi-static isotropic compression, dropping from 5% to 0.5% approximately.

From the perspective of classical continuum mechanics, there does not exist rotation over the isotropically compressed sample. However, the imbalance of internal and external moments of the DEM RVE that undergoes a quasi-static process indicates an overall rotation or spin of the RVE, which results in an asymmetric stress tensor. In this example, the overall rotation can be delineated at a characteristic length that matches the RVE dimensions. In general, the characteristic length may be smaller than that. The Cauchy stress tensor symmetry is only an assumption for macroscale problems in which the microstructure can be neglected (Lin and Wu, 2016).
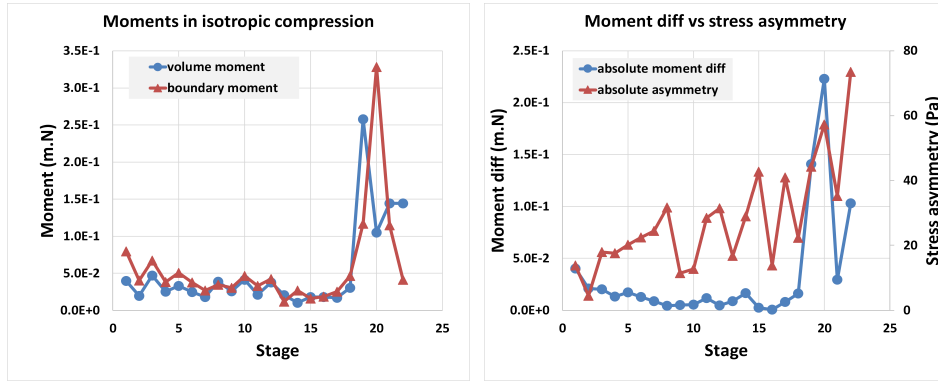
(a) Moment.

(b) AA.
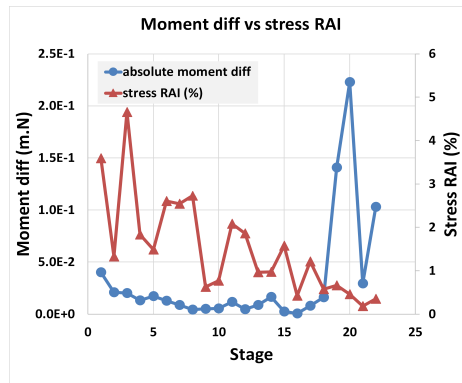
(c) RAI.

Figure 13: Moment and stress asymmetry in isotropic compression.

32

5.5. Quasi-static oedometer compression

A quasi-static uniaxial compression is applied to the gravitationally deposited particle assembly composed of 7,093 monodispersed ellipsoidal particles in a rigid container, as shown in Fig.14. The friction between the rigid walls and particles is assumed to be zero. The top wall moves downward at a constant low speed of 1.5E-5 m/s (loading stage) and stops when the axial strain reaches 25% (resting stage).
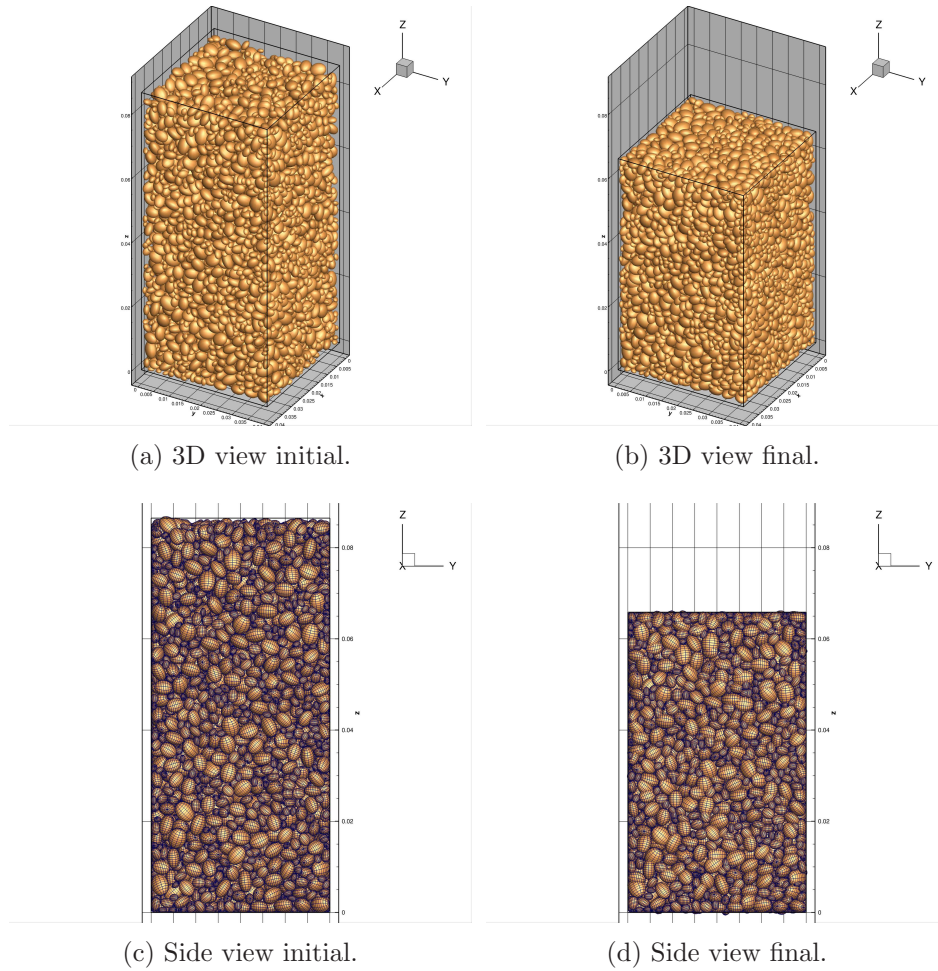

(a) 3D view initial.

(b) 3D view final.

(c) Side view initial.

(d) Side view final.

Figure 14: Oedometer compression of 7,093 monodisperse ellipsoidal particles.

Figure 15(a) shows that the average normal force, average shear force and average contact penetration between particles increase in the process of

oedometer compression. They increase faster at early stage and slow down at late stage. The energy process reveals the same trend as shown in Fig.15(b). The tractions on the six walls of the rigid container are plotted in Fig.15(c): they increase in the compression process; the top and bottom wall tractions fluctuate at the instant of strain termination, and rest eventually. Beware the time shown in Fig.15(b,c) only represents numerical meaning in quasi-static simulations.
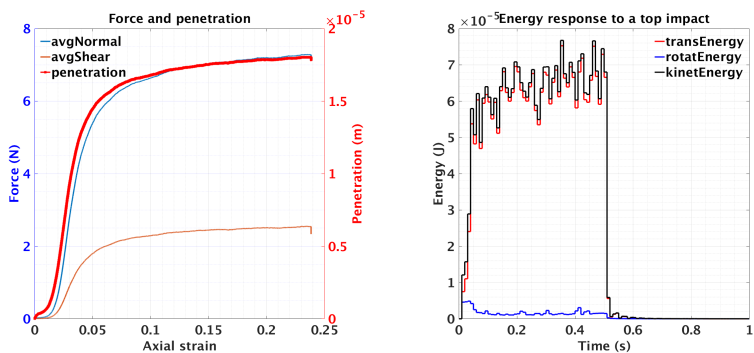
(a) Internal forces.
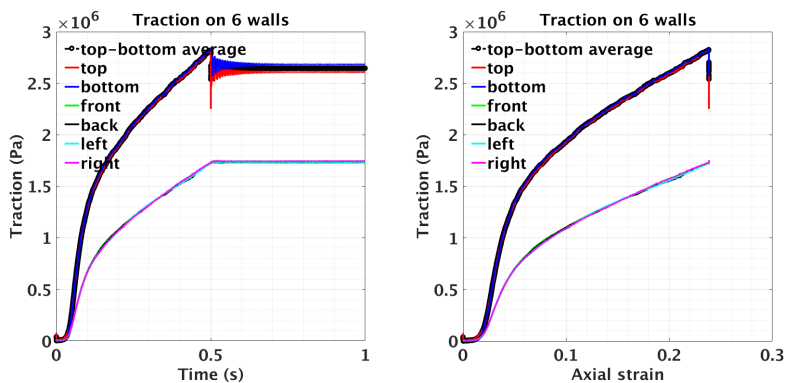
(b) Energy.

(c) Tractions

Figure 15: Force, energy and traction in quasi-static oedometer compression.

Table 7 lists the 3x3 matrices of modified Nicot stress tensor at stages 10, 30, 52 and 90 of 100 snapshots in the simulation process. The stress tensors

exhibit fairly good symmetry for these stages, but they are actually higher if checked in Fig.16(c).

Table 7: Stress tensor calculated from oedometer compression

stage	stress tensor			RAI (%)	AA
10	-6.64E+05	2.16E+02	3.44E+03	0.97	7.60E+01
	2.52E+02	-6.59E+05	1.74E+03		
	3.41E+03	1.68E+03	-1.28E+06		
30	-1.32E+06	-6.47E+03	1.41E+04	0.41	1.57E+02
	-6.60E+03	-1.30E+06	6.81E+03		
	1.42E+04	6.81E+03	-2.26E+06		
52	-1.74E+06	1.75E+03	1.49E+04	0.21	7.78E+01
	1.74E+03	-1.73E+06	1.02E+04		
	1.48E+04	1.02E+04	-2.67E+06		
90	-1.74E+06	1.47E+03	1.34E+04	0.06	1.98E+01
	1.47E+03	-1.73E+06	9.70E+03		
	1.34E+04	9.69E+03	-2.66E+06		

Figure 16(a) plots the volume and boundary moments, which correspond to the LHS and RHS of Eq.(23), respectively, during the process of oedometer compression. It is clear that the volume and boundary moments are not exactly the same, and in particular, they differ substantially after the strain termination.

As pointed out in Section 4.3.1, global damping in DEM may result in inaccurate computation of linear and angular momenta of the RVE particles, so only interparticle contact damping is applied in combination with particle mass scaling in order to achieve quasi-static simulations. Such a damping mechanism allows capture of stress wave after the strain termination: the top and bottom boundary tractions differentiate but converge eventually, as indicated by Fig.15(c). It is interesting to find from Fig.16(a,b) that the difference between internal and external moments jumps up at the instant of strain termination, which exactly reflects the stress wave propagation effect.

Again, there does not exist rotation over the oedometerly compressed sample in the sense of classical continuum mechanics, but the imbalance of internal and external moments implies an overall rotation or spin of the sample, which results in an asymmetric stress tensor.

Figure 16(b) shows the difference between volume and boundary moments and absolute asymmetry (AA) of stress according to Eq.(25). It is observed that moment difference is very low while AA is high in loading stage, and moment difference is high while AA is very low in resting stage. From Fig.16(c) it is observed that RAI exhibits a similar overall trend as AA, but it decreases in the loading stage.

35
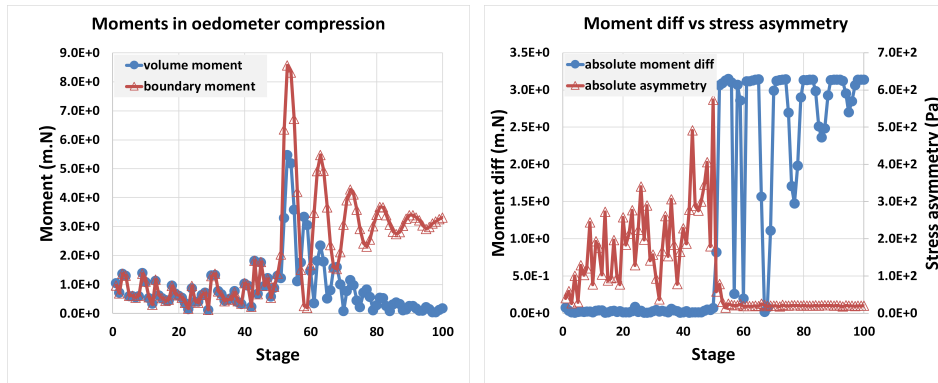
(a) Moment.

(b) AA.
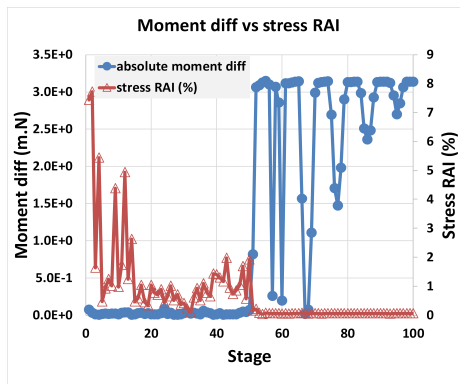
(c) RAI.

Figure 16: Moment and stress asymmetry in oedometer compression.

5.6. High-strain-rate (HSR) oedometer impact

A HSR uniaxial impact is now applied to the same assembly composed of 7,093 monodispersed ellipsoidal particles in a rigid container. The friction between the rigid walls and particles is assumed to be zero. The top wall moves downward at a constant high strain rate (250 /s) and stops when the axial strain reaches 25%. Only the loading stage of 1 ms is simulated.
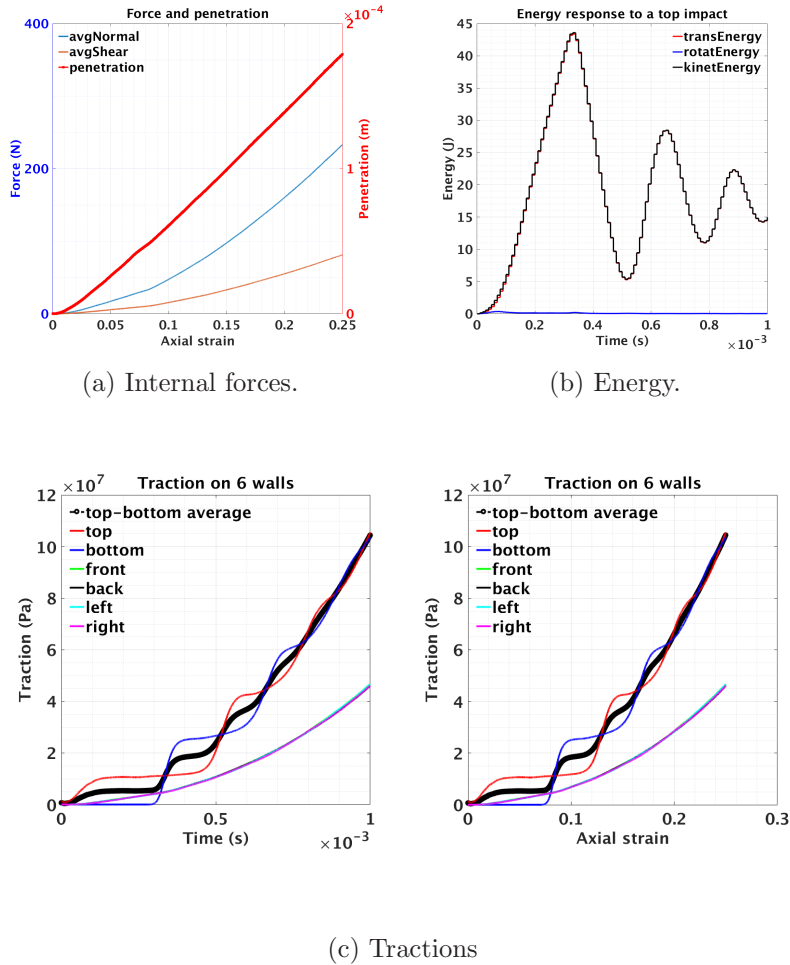

(a) Internal forces.

(b) Energy.

(c) Tractions

Figure 17: Force, energy and traction in HSR oedometer compression.

Figure 17(a) shows that the average normal force, average shear force and average contact penetration between particles increase in the process of impact. The energy process is revealed in Fig.17(b): the kinetic energy of

the particle assembly exhibits a flucutating process with decreasing magnitude, and the rotational energy is nearly negligible. The tractions on the six walls of the rigid container are plotted in Fig.17(c): they increase in the impact process; the top and bottom wall tractions reveal that the stress wave propagation and reflection in the vertical direction of the particle assembly.

Table 8: Stress tensor calculated from HSR impact.

| stage	stress tensor			RAI (%)	AA	inertial term ratio
20	-2.38E+06	-8.47E+03	3.15E+04	2.07	4.48E+03	3.50E-04
	-9.51E+03	-2.32E+06	9.12E+04			
	3.15E+04	8.69E+04	-5.00E+06			
40	-7.09E+06	9.64E+03	-7.37E+04	5.70	5.65E+03	1.04E-04
	9.10E+03	-7.02E+06	-2.68E+03			
	-7.09E+04	2.23E+03	-1.62E+07			
60	-1.58E+07	-1.18E+04	-8.21E+04	3.22	4.71E+03	8.50E-05
	-1.61E+04	-1.56E+07	-3.13E+04			
	-8.13E+04	-2.97E+04	-3.70E+07			
80	-2.86E+07	-9.73E+03	-1.93E+05	1.90	2.94E+03	1.70E-05
	-1.20E+04	-2.85E+07	-1.22E+05			
	-1.91E+05	-1.21E+05	-6.64E+07			

Table 8 lists the 3x3 matrices of Nicot stress tensor at stages 20, 40, 60 and 80 of 100 snapshots in the simulation process. The RAI's are clearly higher than that in the quasi-static oedometer compression. The L^2-norm ratios between inertial terms and stress tensor for the 4 stages are 3.5E-4, 1.0E-4, 8.5E-5, 1.7E-5, respectively: the inertial terms are negligible in HSR oedometer impact.

Figure 18(a) plots the volume and boundary moments during the high-strain-rate impact process: they agree overall, however they differ slightly as seen in Fig.18(c). There is no clear relationship between moment difference and AA shown in Fig.18(b). From Fig.18(c) it is seen the RAI is decreasing even though the moment difference remains in late stage.

Although they look the same in Fig. 18(a) , the internal and external moments in the HSR impact test still differ, as shown in Fig. 18(b). The imbalance of internal and external moments in this dynamic process implies an overall rotation of the sample and results in asymmetric stress tensors.
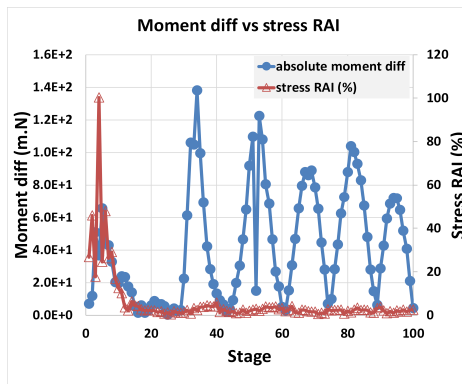
5.7. Stress tensor in discontinuous state

Stress tensor in out-of-contact or "gapped" states is examined by checking different stages of gravitational deposition of 3,456 monodisperse spherical particles into a rigid container. The simulation time is reduced to 1/5 of that shown in Fig.7(b) in order to observe more details. One hundred snapshots
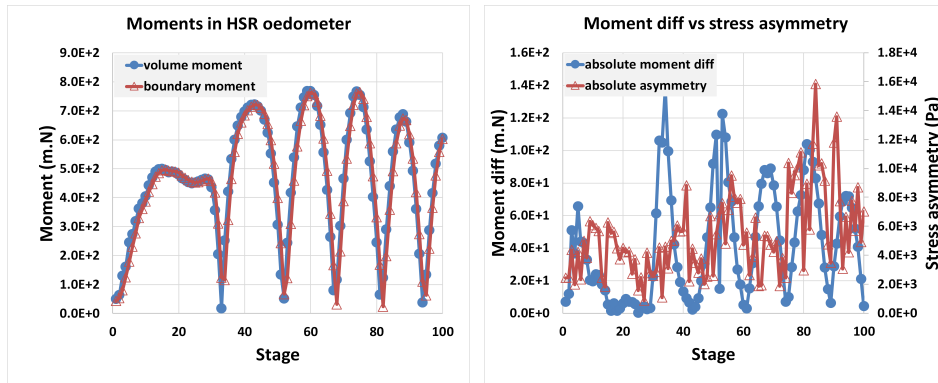
(a) Moment.

(b) AA.

(c) RAI.

Figure 18: Moment and stress asymmetry in HSR oedometer impact.

are taken at equal time interval in the process, and Fig.19 illustrates six of them: 001-initial, 005-deposit, 006-deposit, 009-rebound, 010-rebound and 100-rested.
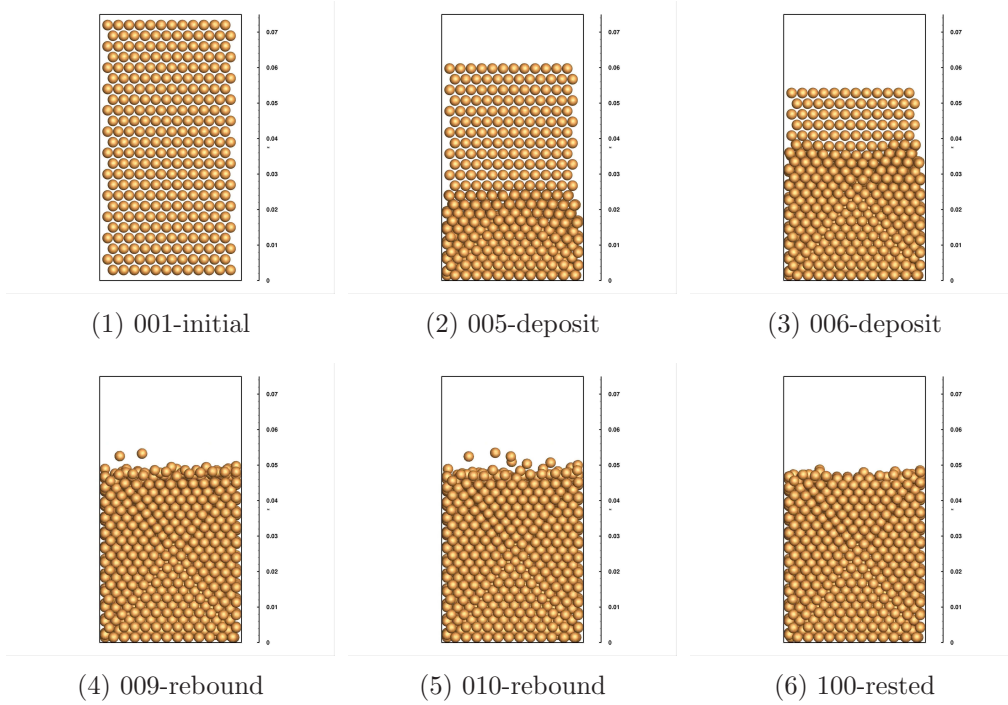

(1) 001-initial   (2) 005-deposit   (3) 006-deposit

(4) 009-rebound   (5) 010-rebound   (6) 100-rested

Figure 19: Sequential snapshot of gravitational deposition, rebound and rest.

Table 9 lists stress tensors calculated by Nicot's formula at the instant of the four snapshots. It is zero at the initial stage when the particles have not formed any contacts; at stage 005, some particles have packed at the bottom of the container while some are still free falling, the stress tensor is asymmetric and RAI is as high as 9.2%; at stage 010, most particles have packed while some particles are rebounding above the surface of the particle assembly, the stress tensor is asymmetric but close to symmetric (RAI is 1.7%); in the rested state (stage 100), the stress exhibits excellent symmetry.

Figure 20(a) plots the volume and boundary moments during the process of gravitational deposition. It is seen that the volume and boundary moments differ at the stages of deposition, packing and rebound, but they become equal at the rested stage. Figure 20(b) reveals that absolute asymmetry (AA) of stress decreases with the decreasing moment difference, and it becomes nil
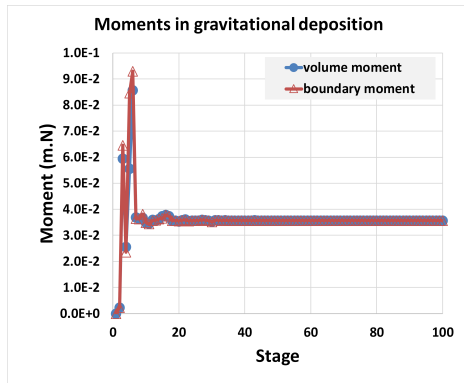
(a) Moment.
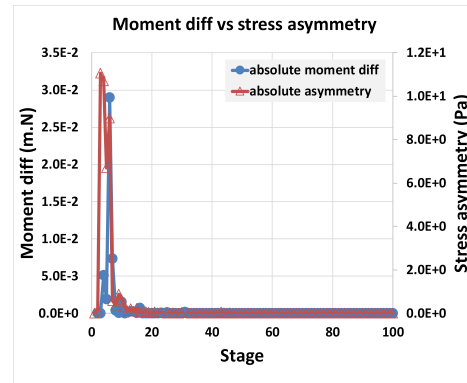
(b) AA.
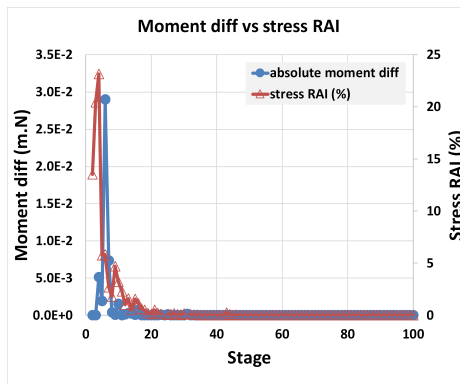
(c) RAI.

Figure 20: Moment and stress asymmetry in gravitational deposition.

Table 9: "Stress" at various stages of gravitational deposition.

stage	stress tensor			RAI (%)
001	0.00E+00	0.00E+00	0.00E+00	0
	0.00E+00	0.00E+00	0.00E+00	
	0.00E+00	0.00E+00	0.00E+00	
005	-2.63E+02	-7.72E+00	-2.81E+01	9.2
	-3.53E+00	-2.64E+02	-1.28E+01	
	-2.88E+01	-8.58E+00	-4.73E+02	
006	-5.38E+02	-2.69E+01	8.52E+01	2.7
	-2.54E+01	-5.28E+02	6.42E+01	
	8.69E+01	5.82E+01	-7.64E+02	
009	-2.21E+02	9.56E+00	-2.57E+00	1.5
	9.62E+00	-2.21E+02	-3.57E+00	
	-2.91E+00	-3.61E+00	-3.43E+02	
010	-2.15E+02	1.07E+01	-3.53E+00	1.7
	1.07E+01	-2.14E+02	-3.32E+00	
	-3.68E+00	-2.92E+00	-3.28E+02	
100	-2.47E+02	1.10E+01	-1.98E+00	0
	1.10E+01	-2.48E+02	-1.64E+00	
	-1.98E+00	-1.64E+00	-3.79E+02	

when the latter becomes zero. Figure 20(c) shows that the RAI decreases during the process: it is 23% at depositing stage and becomes nil at rested state.

As pointed out in Section 4, the stress tensor is defined only when the granular medium is in "continuous" state. When the granular medium is in out-of-contact state, like stages 005 or 010 (partially in-contact and partially out-of-contact), the calculated stress only represents a numerical value, losing its original mechanical implication. However, it still provides a measure of stress. The question is whether to adjust the RVE domain, and split into two: (i) gapped, (2) not-gapped.

6. CONCLUSION AND OUTLOOK

Based on the analytical and numerical work in the paper, the following conclusions can be made:

- Weber's, Drescher's and Bagi's formulas are not equivalent for static equilibrium.
- There are three important reasons for the *boundary-radius-gap* term to be not neglected: wide range of particle sizes in some granular materials, relatively small number of particles needed in a RVE for accurate stress tensor calculation, and symmetry attribute of stress tensor.

- From the perspective of stress tensor calculation, the number of particles in the RVE does not need to be large, namely, tens or hundreds of particles would be adequate provided that high-precision contact geometric resolution is assured.
- Cauchy's stress theorem is not accurately satisfied using averaged stress tensor defined for granular media, or for other materials with "granular" microstructure, such as polycrystalline metals. The averaged stress tensor is more like a quantity that is obtained for a microelement or microvolume in micropolar continuum theory, rather than a pointwise value in classical continuum mechanics.
- The inertial terms in the averaged stress tensor are nearly negligible in quasi-static compression and dynamic impact.
- Any form of deformation of granular media implies or includes rotation, which is an essential difference from classical continuum mechanics. To define the rotation and associate it to stress in granular media may need micropolar continuum theory.
- Symmetry of averaged stress tensor calculated from DEM RVEs can be accurately satisfied in static equilibrium; however, it cannot in quasi-static or dynamic states due to imbalance of angular momentum over the discrete RVEs.
- The stress tensor is normally defined when the granular medium is in a "continuous" state. When it is extended to "discontinuous" or "gapped" state, the calculated stress may lose its original mechanical interpretation.

It is clealy seen from Section 5 that the imbalance of angular momentum exists under quasi-static and dynamic loading conditions for discrete granular media mechanics via 3D DEM RVE simulations, and it results in asymmetry of the averaged stress tensor. This phenomenon is not easily interpreted by classical continuum mechanics, as pointed out by Eringen (1968): " If the response of the body to an external physical effect is sought, in which the length scale is comparable to the average grain or molecular size contained in the body, the granular or molecular constituents of the body are excited individually. In this case, the intrinsic motions of the constituents (microelements) must be taken into account. This point becomes clear especially in connection with the propagation of waves having high frequencies or short wavelengths. When the wavelength is of the same order of magnitude as the average dimension of the microelements, the intrinsic motions of the mi-

croelements of ΔV with respect to the center of mass of ΔV can affect the response appreciably."

In micropolar continuum theory, Cauchy's stress tensor is asymmetric in general, and the imbalance of angular momentum of classical continuum mechanics is generalized to include terms (surface couple, body couple and intrinsic spin) such that they become balanced.

It is of great interest to extend the averaged stress and relevant rate form tensors to large-scale parallel computing of 3D DEM for granular materials (which normally provides adaptive compute grids for particle assembly partitioning), and upscale the granular medium to continuum for study of stress-strain relations. A proper implementation and application of the averaged stress tensor in domain-decomposed parallelism of 3D DEM relies on the stress definition and requires careful treatment. For example, if Bagi's formula is adopted, it is not only necessary to collect boundary-particle contact information, but also requires processing particle-particle contact information between adjacent compute grids and define branch vectors accurately; if Weber's formula is adopted, then it becomes unnecessary to do so.

Acknowledgments

Katalin Bagi. Stress and strain in granular assemblies. *Mechanics of materials*, 22(3):165–177, 1996.

Katalin Bagi. Microstructural stress tensor of granular assemblies with volume forces. *Journal of Applied Mechanics*, 66(4):934–936, 1999.

Katalin Bagi. Discussion on the asymmetry of stress in granular media by jp bardet and i. vardoulakis:[int. j. solids and structures, vol. 38, pp. 353–367 (2001)]. *International Journal of Solids and Structures*, 40(5):1329–1331, 2003.

R Balevičius and D Markauskas. Numerical stress analysis of granular material. *Mechanics*, 66(4):12–17, 2007.

JP Bardet and I Vardoulakis. The asymmetry of stress in granular media. *International Journal of Solids and Structures*, 38(2):353–367, 2001.

C. Chree. Changes in the dimension of elastic bodies due to given systems of forces. *Cambridge Philos. Soc. Trans.*, 15:313337, 1892.

J. Christoffersen, M.M. Mehrabadi, and S. Nemat-Nasser. A micromechanical description of granular material behavior. *Trans. ASME, J. App. Mech.*, 48:339–344, 1981.

SC Cowin. Effective stress strain relations for finitely deformed inhomogenous bodies. *Mechanics Research Communications*, 4(3):163–169, 1977.

PA Cundall and ODL Strack. Modeling of microscopic mechanisms in granular material. In *Studies in Applied mechanics*, volume 7, pages 137–149. Elsevier, 1983.

Gery De Saxcé, Jérôme Fortin, and Olivier Millet. About the numerical simulation of the dynamics of granular media and the definition of the mean stress tensor. *Mechanics of Materials*, 36(12):1175–1184, 2004.

A Drescher and G De Josselin De Jong. Photoelastic verification of a mechanical model for the flow of a granular material. *Journal of the Mechanics and Physics of Solids*, 20(5):337–340, 1972.

A.C. Eringen. Theory of Micropolar Elasticity. In H. Liebowitz, editor, *Fracture, An Advanced Treatise*, volume 2, pages 622–729. Academic Press, 1968.

Jérôme Fortin, Olivier Millet, and Gery De Saxcé. Construction of an averaged stress tensor for a granular medium. *European Journal of Mechanics-A/Solids*, 22(4):567–582, 2003.

Fatih Göncü and Stefan Luding. Effect of particle friction and polydispersity on the macroscopic stress–strain relations of granular materials. *Acta geotechnica*, 8(6):629–643, 2013.

S. W. Key, C. M. Stone, and R. D. Krieg. Dynamic relaxation applied to the quasi-static, large deformation, inelastic response of axisymmetric solids. 1980. ERDA/420200;.

Matthew R Kuhn. Discussion of the asymmetry of stress in granular media:[jp bardet and i. vardoulakis, int. j. solids struct. 2001, vol. 38, no. 2, pp. 353–367]. *International journal of solids and structures*, 40(7):1805–1807, 2003.

Jia Lin and Wei Wu. Asymmetry of the stress tenor in granular materials. *Powder Technology*, 293:113–120, 2016.

Jia Lin, Wei Wu, and Ronaldo I Borja. Micropolar hypoplasticity for persistent shear band in heterogeneous granular materials. *Computer Methods in Applied Mechanics and Engineering*, 289:24–43, 2015.

François Nicot, Nejib Hadda, Mohamed Guessasma, Jerome Fortin, and Olivier Millet. On the definition of the stress tensor in granular media. *International Journal of Solids and Structures*, 50(14):2508–2517, 2013.

W Nowacki. The linear theory of micropolar elasticity. In *Micropolar Elasticity*, pages 1–43. Springer, 1974.

Witold Nowacki and Wacław Olszak. *Micropolar Elasticity: Symposium Organized by the Department of Mechanics of Solids, June 1972*, volume 151. Springer, 2014.

Mehdi Omidvar, Magued Iskander, and Stephan Bless. Stress-strain behavior of sand at high strain rates. *International journal of impact engineering*, 49:192–213, 2012.

L. Rothenburg and A.P.S. Selvadurai. Micromechanical definition of the Cauchy stress tensor for particulate media. In A.P.S. Selvadurai, editor, *Mechanics of Structured Media*, pages 469–486. Elsevier Scientific, 1981.

AL Smith and CM Wensrich. The effects of particle dynamics on the calculation of bulk stress in granular media. *International Journal of Solids and Structures*, 51(25-26):4414–4418, 2014.

P. Underwood. Dynamic relaxation. In T. Belytschko and T.J.R. Hughes, editors, *Computational Methods for Transient Analysis*, pages "245–65". North-Holland, Amsterdam, 1983.

J Weber. Recherches concernant les contraintes intergranulaires dans les milieux pulvérulents. *Bulletin de Liaison des Ponts-et-chaussées*, 20:1–20, 1966.

Beichuan Yan. Three-dimensional discrete element modeling of granular materials and its coupling with finite element method. Technical report, Thesis (Ph.D.)–University of Colorado, 2008.

Beichuan Yan and Richard Regueiro. Large-scale dynamic and static simulations of complex-shaped granular materials using parallel three-dimensional discrete element method (dem) on dod supercomputers. *Engineering Computations*, 35(2):1049–1084, 2018a.

Beichuan Yan and Richard A Regueiro. A comprehensive study of mpi parallelism in three-dimensional discrete element method (dem) simulation of complex-shaped granular particles. *Computational Particle Mechanics*, 5 (4):553–577, 2018b.

Beichuan Yan, Richard A Regueiro, and Stein Sture. Three-dimensional ellipsoidal discrete element modeling of granular materials and its coupling with finite element facets. *Engineering Computations*, 27(4):519–550, 2010.